
SUPPORTING INFORMATION

Engineering first-order spin-orbit coupling in a pentagonal bipyramidal Fe(II) complex and subsequent SMM behavior

Kateryna Bretosh,^a Virginie Béreau,^{a,b} Flaurant Heully-Alary,^c Nicolas Suaud,^{c,*} Carine Duhayon,^a Elen Duverger-Nédellec,^d Nathalie Guihéry,^{c,*} Jean-Pascal Sutter*,^a

CONTENT

| | |
|---|------|
| EXPERIMENTAL | S2 |
| Crystallographic studies for $[\text{FeL}^{\text{N5}}\text{Cl}_2]\cdot 3\text{H}_2\text{O}$, 2 : | S3 |
| Table S1. Crystallographic data for 1-4 , $[\text{ZnL}^{\text{N5}}\text{Br}]\cdot \text{Br}\cdot 0.5\text{H}_2\text{O}$, and $[\text{ZnL}^{\text{N5}}\text{I}_2]$. | S7 |
| Figure S1. $[\text{FeL}^{\text{N5}}(\text{H}_2\text{O})\text{Cl}]\text{Cl}\cdot 4.5\text{H}_2\text{O}$, 1 : ORTEP plot, lattice organization, and selected inter-atomic distances. | S8 |
| Figure S2. $[\text{FeL}^{\text{N5}}\text{Cl}_2]\cdot 5\text{H}_2\text{O}$, 2 : ORTEP plot, crystal packing, and selected inter-atomic distances and angles | S10 |
| Figure S3. $[\text{FeL}^{\text{N5}}\text{Br}_2]$, 3 : ORTEP plot, crystal packing, and selected inter-atomic distances. | S11 |
| Figure S4. $[\text{FeL}^{\text{N5}}\text{I}_2]$, 4 : ORTEP plot, crystal packing, and selected inter-atomic distances. | S13 |
| Figure S5. $[\text{ZnL}^{\text{N5}}\text{I}_2]$: molecular complex, crystal packing, and selected inter-atomic distances. | S15 |
| Figure S6. $[\text{ZnL}^{\text{N5}}\text{Br}]\text{Br}\cdot 0.5\text{H}_2\text{O}$: crystal packing, and selected inter-atomic distances. | S16 |
| Table S2. Results of SHAPE analysis | S16 |
| Figure S7. PXRD for 1 , 3-5 , $[\text{ZnL}^{\text{N5}}\text{I}_2]$, and $[\text{ZnL}^{\text{N5}}\text{Br}]\text{Br}\cdot 0.5\text{H}_2\text{O}$. | S 17 |
| Figure S8. Mössbauer spectra for 1 , 3 , and 4 | S19 |
| Figure S9. Energy dispersive X-ray (EDX) analysis for $[\text{Fe}_{0.12}\text{Zn}_{0.88}\text{L}^{\text{N5}}\text{I}_2]$, 5 . | S20 |
| Figure S10. M versus H at 2-8 K 1 for 1 , 3- 5 . | S21 |
| Figure S11. AC magnetic susceptibility for 1 . | S22 |
| Figure S12. AC magnetic susceptibility for 3 . | S23 |
| Table S3. Best-fit parameters of the analyses of χ_M'' versus ν by a generalized Debye model for 3 . | S24 |
| Figure S13. AC magnetic susceptibility for 4 . | S25 |
| Table S4. Best-fit parameters of the analyses of χ_M'' versus ν by a generalized Debye model for 4 : a) no applied static field, b) with $H_{\text{DC}} = 5$ kOe. | S28 |
| Figure S14. AC magnetic susceptibility for 5 . | S29 |
| Table S5. Best-fit parameters of the analyses of χ_M'' versus ν ($H_{\text{DC}} = 1$ kOe) by a generalized Debye model for 5 | S30 |
| Table S6. Matrix representative of the spin-orbit Hamiltonian of equation 2. | S31 |
| Table S7. Matrix representative of the ZFS Hamiltonian given in equation 4. | S31 |
| Table S8. Values for g_x , g_y , and g_z of complexes 1-4 . | S31 |
| Figure S15. View of the D tensor proper axes, x in red, y in green, and z in blue of complexes 1-4 . | S32 |
| REFERENCES | S33 |

EXPERIMENTAL

Fourier transform infrared (FT-IR) spectroscopy was performed in the 4000-600 cm^{-1} range with a Perkin–Elmer spectrum GX 2000 FT-IR spectrometer using the ATR mode. Elemental analyses were performed with a Perkin–Elmer 2400 series II instrument.

Mössbauer measurements were recorded at 80 K by using an MD 306 Oxford cryostat on a constant acceleration conventional spectrometer with a 50 mCi source of ^{57}Fe (Rh matrix). The absorber was a microcrystalline powder sample (20-50 mg) enclosed in a 20 mm diameter cylindrical, plastic sample holder; the size of which had been determined to optimize the absorption. The hyperfine parameters were obtained by least-squares fitting to Lorentzian lines. Isomer shift values (δ) are relative to iron foil at 293 K.

Magnetic studies were carried out with a Quantum Design MPMS-5S SQUID magnetometer on freshly isolated polycrystalline powders put in gelatin capsules mixed to grease. Data have been collected between 300 and 2 K with an applied field of 1 kOe and corrected for the diamagnetic contribution sample by using Pascal's tables¹ and for the sample holder. The field dependences of the magnetization were measured between 2 and 8 K with dc magnetic field up to 5 T. AC susceptibility data were collected with $H_{AC} = 3$ Oe in the frequency range 1–1500 Hz. Assessment of the ZFS parameters have been done considering an $S = 2$ spin for Fe(II), the software PHI^{2, 3} was used for fitting the $\chi_M T = f(T)$ and $M = f(H)$ behaviors.

Powder X-Ray diffraction (PXRD) patterns were recorded in transmission mode, using capillary tubes filled with slightly crushed crystals in their growing solution, on a *SmartLab* (Theta–Theta mode) Rigaku diffractometer, or in reflection mode with slightly crushed crystals on a Miniflex600 Rigaku diffractometer (Theta-2Theta mode) with $\lambda(\text{Cu}_{K\alpha 1, K\alpha 2}) = 1.54059$ and 1.54439 Å.

High Resolution Transmission Electronic Microscopy (TEM): A JEOL JSM 2100F High Resolution Transmission Electron Microscope operating at 200 kV was used (resolution of 2.3 Å). The numerical analysis of the images was performed with CMOS Gatan RIO16IS 4K*4K camera. An Ultim Max TEM Windowless detector by Oxford Instruments (sensor size 80mm²) was used for the EDX analysis. The sample was prepared in acetone and deposited on a Cu grid.

Synthesis of the Zn derivative: The reaction have been performed in atmospheric conditions with commercial or prepared reagents used as obtained.

[ZnL^{N5}Br]Br.0.5H₂O Phen^{MeNH2}.2HCl (150.0 mg; 0.44 mmol) was suspended in a mixture of 15 mL H₂O and 15 mL of methanol. Then, Zn(OAc)₂.2H₂O (126.0 mg; 0.57 mmol) was added, the solution turned yellow clear without any insoluble. The further addition of 2,6-diacetylpyridine (91.0 mg; 0.56 mmol) and 3 drops of 48% HBr aqueous solution gave a bright yellow solution that was heated to reflux for 3h30. At the end of the heating time, NaBr (460.0 mg; 4.50 mmol) was added to the hot solution let to concentrate to 15 mL at room temperature. Yellow crystals suitable for X-Ray diffraction were filtered, washed with water and dried with acetone and under vacuum (160.0 mg, 57%). Elemental analysis: calcd for C₂₃H₂₁N₇Br₂ZnO (with 1 H₂O molecule as solvent) C, 43.25; H, 3.63; N, 15.35. Found C, 43.05; H, 2.85; N, 15.24. IR (ν_{max} / cm^{-1}): 3362w, 3049w, 3001w, 2939w, 1615w, 1591vs, 1570w, 1496s, 1485s, 1423w, 1362s, 1311w, 1256w, 1218w, 1188s, 1153s, 1089s, 1033s, 957w, 859s, 814w, 796s, 745w, 690w, 653w.

ZnL^{N5}I₂ Phen^{MeNH2}.2HCl (85.0 mg; 0.25 mmol) was suspended in a mixture of 7 mL H₂O and 7 mL of methanol. Then, Zn(NO₃)₂.6H₂O (75.0 mg; 0.25 mmol) was added, the solution turned yellow clear

without any insoluble. The further addition of 2,6-diacetylpyridine (41.0 mg; 0.25 mmol) and 2 drops of 47% HI aqueous solution gave a bright yellow solution that was heated to reflux for 3h. At the end of the heating time, NaI (225.0 mg; 1.50 mmol) was added to the hot solution that lead to the precipitation of a yellow solid. After cooling down to room temperature, the yellow solid was isolated by filtration, washed with ethanol and dried with diethyl ether (136.0 mg, 76%). Yellow crystals suitable for X-Ray diffraction were obtained by slow evaporation of the filtrate. Elemental analysis: calcd for $C_{23}H_{21}N_7I_2Zn$ C, 38.65; H, 2.96; N, 13.75. Found C, 38.40; H, 2.16; N, 13.64. IR (ν_{max}/cm^{-1}): 3473w, 3038w, 3001w, 1615w, 1592vs, 1574w, 1497s, 1479s, 1411w, 1359s, 1300w, 1252w, 1216w, 1184s, 1150w, 1094s, 1035vs, 953w, 870s, 814s, 797s, 746s, 690w, 656w.

Crystallographic studies for $[FeL^{N5}Cl_2] \cdot 3H_2O$, **2**:

Data were processed with the CrysAlis Pro software.⁴ The unit cell was determined as monoclinic with $a = 10.5068(3) \text{ \AA}$, $b = 13.9448(4) \text{ \AA}$, $c = 12.9245(4) \text{ \AA}$, $\beta = 125.620(4)^\circ$. Satellite reflections were indexed using Ewald explorer function of CrysAlis Pro software with the incommensurate modulation vector $\mathbf{q} = 0.6754(4) \mathbf{a}^* + 0.1052(4) \mathbf{c}^*$. Jana2006 software⁵ was used as well to refine the modulation vector with the “indexing” graphic option enabling to represent a projection of all the measured reflections in one cell (Figure 1). Only one order of satellites is observed.

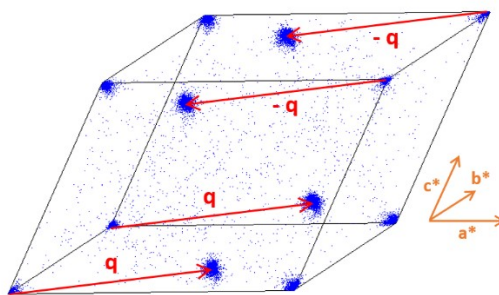


Figure 1: Projection of all the measured reflections into a single monoclinic cell. Reflections at the nodes of the cell are called main reflections and correspond to the average structure of the compound. Additional clusters of reflections, called satellite reflections, are observed in the cell and can be indexed using the incommensurate modulation vector $\mathbf{q} = 0.6754(4) \mathbf{a}^* + 0.1052(4) \mathbf{c}^*$ and its equivalent $-\mathbf{q}$. These satellites represent the periodic deviation from the average structure.

Integration of the data was done without preliminary symmetry assumption except the Laue symmetry, needed for proper frame scaling and absorption correction by spherical harmonic functions (Abspack algorithm from CrysAlis Pro). Study of the reciprocal $(hkl)^*$ layers, reconstructed using the unwarped option in CrysAlis Pro, was done to evidence systematic absences. This analysis revealed a C centering (extinctions for $h + k = 2n+1$), corresponding to a centering vector $(1/2, 1/2, 0, 0)$, as well as an intrinsic translation of $1/2$ along the fourth dimension, *i.e* along the modulation vector, given by the extinctions observed for $h0lm$, $m = 2n+1$ (Figure 2).

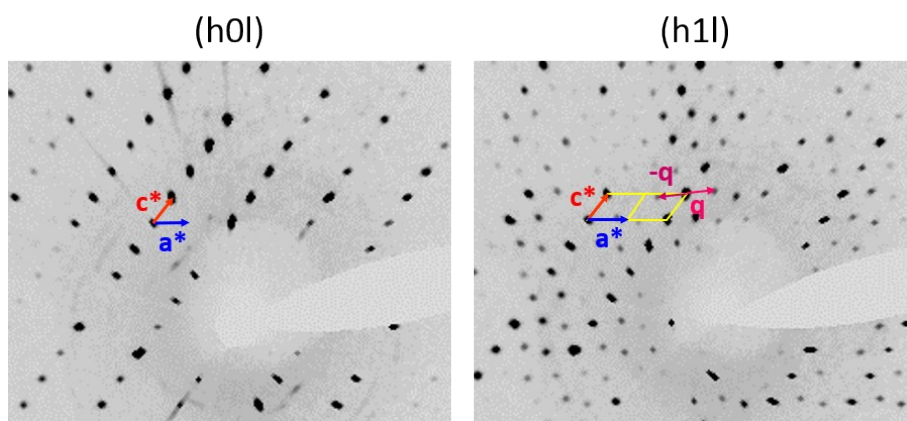


Figure 2: Reciprocal plans reconstruction evidencing systematic extinctions for $h+k=2n+1$, and for $h0lm$, $m = 2n+1$.

The structure was solved by charge flipping methods with Superflip program⁶ using the super-space group $C2/m(a0g)0s$ and refined with Jana2006. A superimposition of two inversed configurations of the complex was obtained as shown Figure 3a. First hypothesis could be that this “disorder” is in fact a hidden order, reflecting a periodic alternation of the two configurations in the crystal along the modulation axis with a periodicity defined by the vector \mathbf{q} . However, the careful look at the Fourier map in the “section” mode evidences that for most positions given by the vector \mathbf{q} there is a coexistence of both configurations (Figure 3b). It means that along the modulation axis a true disorder exists.

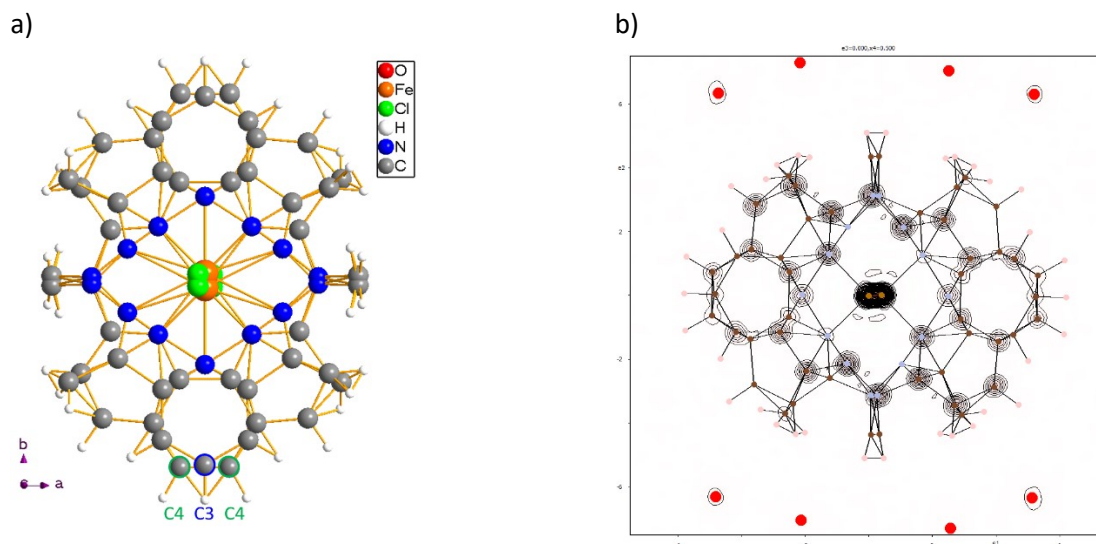


Figure 3: a) The average structure of the compound is composed of a superimposition of two inversed configurations of the iron complex. b) Observed Fourier maps show electronic density corresponding to the atomic positions of both configurations of the complex all along the modulation direction, a true disorder exists in the crystalline structure.

Fourier map verifications were made for each atom to evidence the modulation type, as shown Figure 4. A clear interruption of the observed electronic density along the modulation axis (noted x4) is seen for all the atoms of the complex, meaning that their occupancies are modulated. A displacement along \mathbf{a} and \mathbf{c} (x1 and x3) is evidenced as well; the atoms are then also displaced periodically from their

average position, defined previously by the average structure. To model these modulations 9 parameters to refine per atom are necessary (3 for the occupancy and 6 for the position). However, only one order of satellites was observed and a reliable refinement needs at least 10 observed reflections for 1 refined parameter. To ensure a good quality of the refinement, a rigid body was applied on the carbon, hydrogen and nitrogen atoms of the complex ligands, enabling to apply the same modulation functions to them and reduce the number of parameters to refine to 15 (3 for the occupancy, 3 for translation and 3 for rotation of the rigid body). A positional modulation wave and an occupational modulation wave were applied to the rigid body and to the iron and chloride atoms. A single positional modulation wave was applied to oxygen atoms from the solvent molecules.

The refinement of this model leads to an agreement factor of 6.31% for the main reflections, 8.50% for the satellite reflections and a total agreement factor of 7.30%, evidencing the quality of the refined structure. Difference Fourier maps were checked carefully for all atoms and only weak electronic residues are visible showing the good quality of the model (see Figure 4a).

Each possible configurations and positions of the complex in the sample can be represented by a value of t in the graphs in figure 4b. It is then possible to see that when the occupancy (probability of presence) of C3 is maximal, the one of C4, from the other possible configuration of the complex, is minimal and the displacement of C3 is along \mathbf{b} (dy). And when there is a probability of 50% for each configuration to exist, C3 presents a maximal displacement amplitude along \mathbf{c} (dz) and \mathbf{a} (dx). These modulations can be observed directly on the structure selecting its representation at different values of t , see Figures 5 for positional modulation and Figure 6 for occupancy modulation. A large displacement of the atoms from their average position is observed, up to 0.2 \AA for the carbon atoms at the extremity of the ligands (C3 and C4).

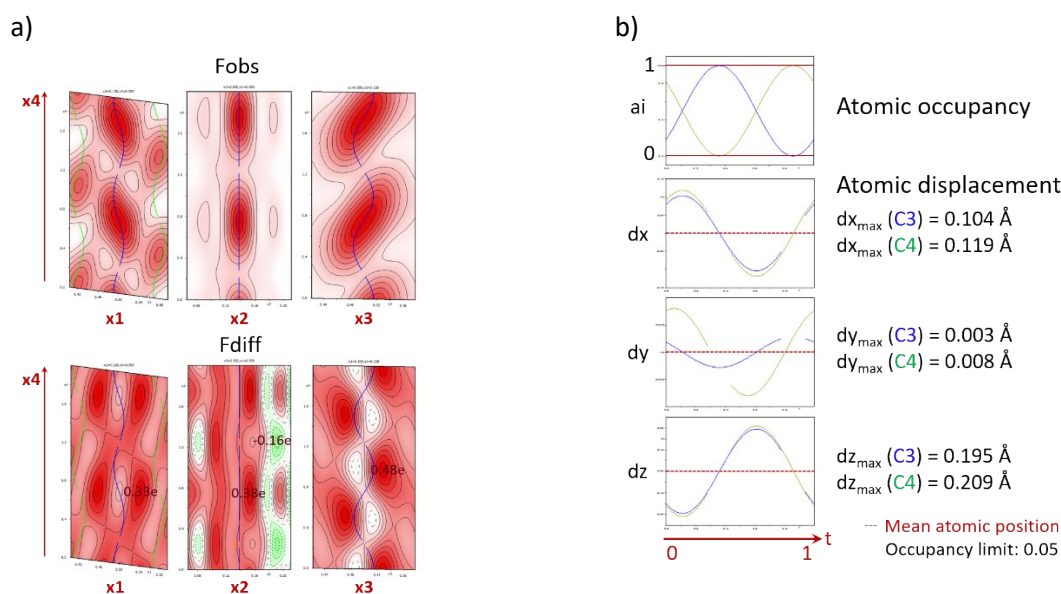


Figure 4: a) Observed and difference Fourier maps generated around the atom C3 (see figure 3a). Position and occupancy of C3 are represented in blue. Position and occupancy of the closest carbon atom belonging to the other configuration, C4, is represented in green. Occupancies lower than 0.05 are not represented. The difference maps show very weak electronic residues, showing that the displacements and the occupancies of C3 and C4 are well modeled. b) Representation of the atomic occupancy and the atomic displacement along \mathbf{a} (dx), \mathbf{b} (dy) and \mathbf{c} (dz) in function of the position t on the modulated axis for C3 (blue) and C4 (green). Each parameter is modeled as a sinusoidal function. Each value of t represents a position in the crystal and then all possible configuration and position of the complex are summarized in these graphs. A large displacement up to 0.2 \AA around the mean position is observed for both of the carbons and can explain the relatively strong intensity of the measured satellite reflections.

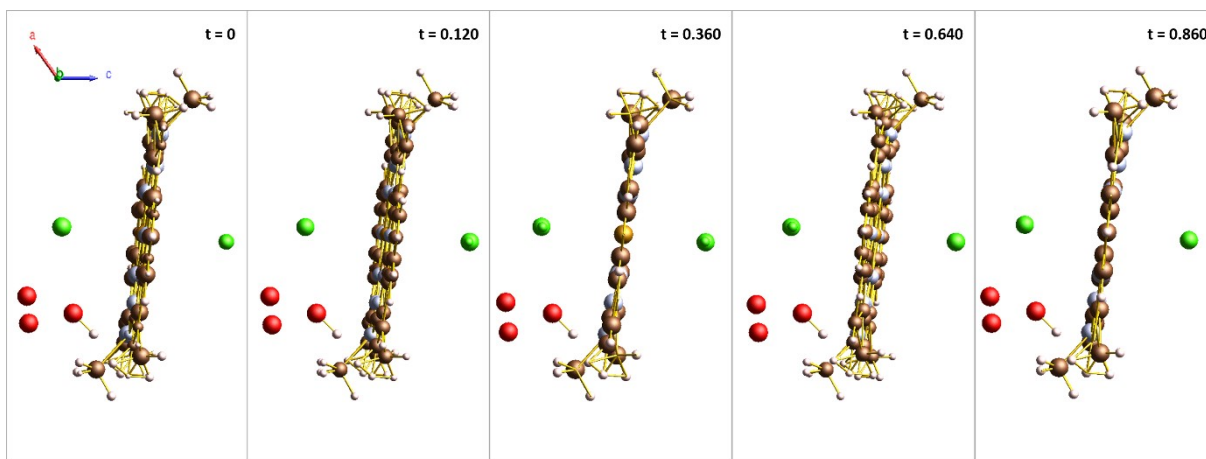


Figure 5: Highlight of the positional modulation presented by the iron complex. A rotation of the molecule is clearly observed when varying t value. The images were generated by the software Jana2020.⁷

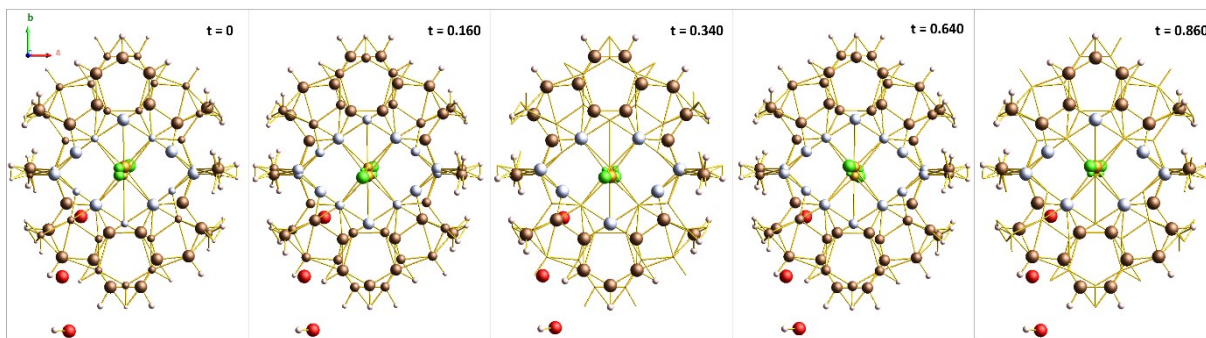


Figure 6: Highlight of the occupancy modulation of the iron complex. The probability of finding one configuration of the complex or the other is represented by the size of their atoms. At $t = 0.340$ the probability of finding the configuration 1 is almost 100%, and at $t = 0.860$, the configuration 1 is not observed. At $t = 0.160$ and $t = 0.640$ there is almost 50% chance of finding the configuration 1 and almost 50% chance of finding the configuration 2. The images were generated by the software Jana2020.⁷

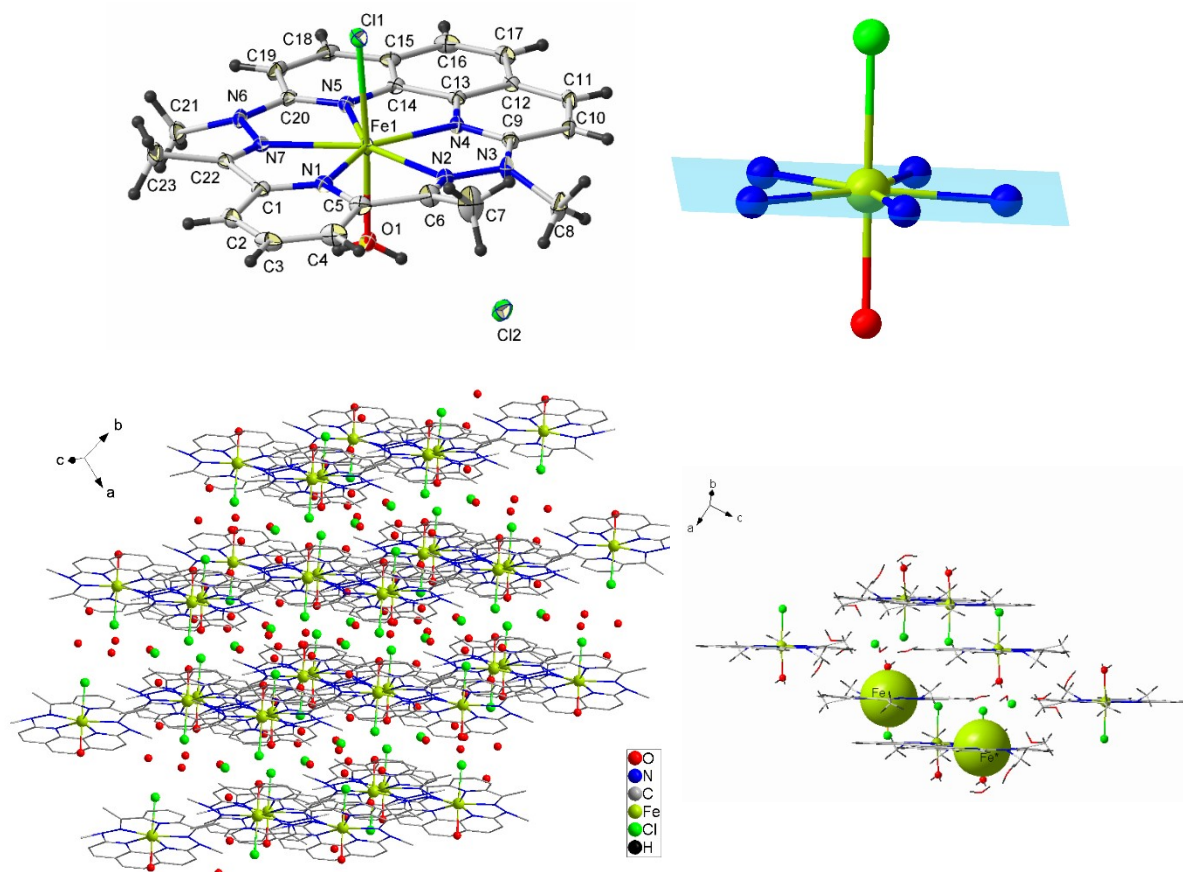
To conclude, the incommensurately modulated structure of this complex was successfully solved and refined in (3+1) dimensions, evidencing an ordered-disorder along the fourth dimension as well as a significant atomic displacement from the average positions.

Table S1. Crystallographic data for **1-4**, **[ZnL^{N5}Br]·Br·0.5H₂O**, and **[ZnL^{N5}I₂]**.

| | 1 | 2 | 3 | 4 | ZnL ^{N5} Br·Br | ZnL ^{N5} I ₂ |
|---|---|--|--|---|--|--|
| Formula | C ₂₃ H ₃₂ Cl ₂ FeN ₇ O _{5.5} | C ₂₃ H ₄₁ Cl ₂ FeN ₇ O ₁₀ | C ₂₃ H ₂₁ Br ₂ FeN ₇ | C ₂₃ H ₂₁ FeI ₂ N ₇ | C ₂₃ H ₂₂ Br ₂ N ₇ O _{0.5} Zn | C ₂₃ H ₂₁ I ₂ N ₇ Zn |
| Mr | 621.30 | 702.36 | 611.12 | 705.12 | 629.66 | 714.66 |
| Crystal system | triclinic | monoclinic | monoclinic | monoclinic | monoclinic | monoclinic |
| Crystal color ^b | yellow | orange | red | dark red | yellow | yellow |
| Space group | P -1 | C2/m | C 2/c | C 2/c | P 2 ₁ /c | C 2/c |
| a/Å | 8.3940(11) | 10.5068(3) ^a | 9.8363(6) | 9.8046(3) | 11.765(2) | 9.83960(2) |
| b/Å | 10.8716(14) | 13.9448(4) ^a | 14.4946(6) | 15.2785(4) | 14.627(3) | 15.20730(3) |
| c/Å | 15.591(2) | 12.9245(4) ^a | 15.0645(8) | 15.4415(5) | 14.454(3) | 15.45460(3) |
| α /° | 104.063(4) | 90 ^a | 90 | 90 | 90 | 90 |
| β /° | 97.237(5) | 125.620(4) ^a | 102.256(2) | 102.293(1) | 113.172(6) | 102.2080(18) |
| γ /° | 103.484(4) | 90 ^a | 90 | 90 | 90 | 90 |
| V/Å ³ | 1316.7(3) | 1539.3(1) ^a | 2098.8(2) | 2260.1(1) | 2286.6(9) | 2260.2(1) |
| Z | 2 | 2 | 4 | 4 | 4 | 4 |
| T/K | 100 | 100 | 100 | 100 | 110 | 135 |
| ρ _{calcd} /gcm ⁻³ | 1.567 | 1.4762 | 1.934 | 2.072 | 1.826 | 2.100 |
| μ(Mo-Kα)mm ⁻¹ | 0.827 | 0.726 | 4.556 | 3.427 | 4.599 | 3.846 |
| Absorption correction | multi-scan | multi-scan | multi-scan | multi-scan | multi-scan | multi-scan |
| T _{min} | 0.86 | 0.67 | 0.79 | 0.45 | 0.51 | 0.74 |
| T _{max} | 0.91 | 0.75 | 0.91 | 0.60 | 0.58 | 0.86 |
| Reflections measured | 40327 | 88445 | 18838 | 52191 | 63455 | 25287 |
| Independent reflections | 7951 | 16861 | 2147 | 2795 | 6970 | 2803 |
| Rint | 0.067 | 0.080 | 0.044 | 0.039 | 0.076 | 0.044 |
| Refl. with I > nσ(I) | 4674 (n=2) | 16861 (9707 main refl., 7154 satellites refl.) n=3 | 1898 (n=2) | 2669 (n=2) | 3875 (n=2) | 2606 (n=2) |
| Nb parameters | 352 | 209 | 153 | 153 | 316 | 153 |
| Nb restraints | 0 | 0 | 4 | 4 | 0 | 4 |
| R ₁ /wR ₂ (I > nσ(I)) | 0.0338/0.0748 | 0.0730/0.1110 | 0.0404/0.0964 | 0.0261/0.0292 | 0.0474/0.1233 | 0.0312/0.0740 |
| Residual e- density (ē·Å ⁻³) | 0.64/-0.64 | 0.59/-0.63 | 2.10/-0.86 | 2.15/-0.58 | 1.45/-1.66 | 4.01/-1.26 |
| CCDC number | 2352840 | 2352845 | 2352841 | 2352842 | 2352843 | 2352844 |

^a Incommensurable structure with modulation vector of 0.6754a + 0.1052c; ^b apparent color under optical microscope

Figure S1. $[\text{FeL}^{\text{N5}}(\text{H}_2\text{O})\text{Cl}]\text{Cl}\cdot 4.5\text{H}_2\text{O}$, **1**: ORTEP plot (50% probability level, lattice solvent not depicted) with numbering scheme, first coordination sphere with plane (in blue) defined by the 5 N atoms in the equatorial sites, lattice organization, and selected inter-atomic distances.



Fe – Fe(1-x, -y, 1-z): 8.3512(1) Å

Selected interatomic distances (Å) and angles (°)

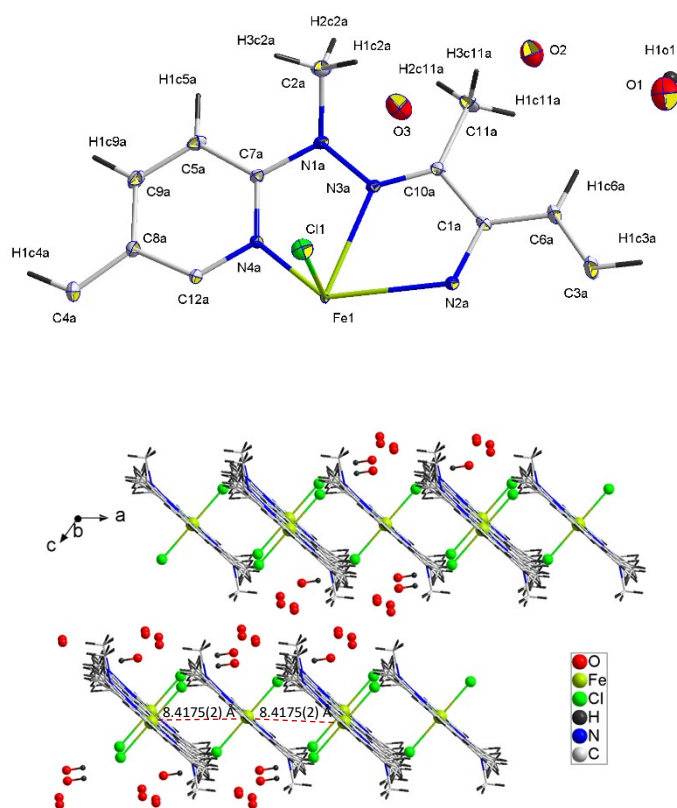
| | | | | | |
|----|-----|-------------|-----|-----|-------------|
| O1 | Fe1 | 2.1930(15)Å | Fe1 | Cl1 | 2.5649(6)Å |
| N1 | C5 | 1.348(3)Å | N1 | C1 | 1.344(3)Å |
| N2 | N3 | 1.381(2)Å | N1 | Fe1 | 2.1125(18)Å |
| N2 | Fe1 | 2.273(2)Å | N2 | C6 | 1.290(3)Å |
| N3 | C9 | 1.394(3)Å | N3 | C8 | 1.474(3)Å |
| N4 | C13 | 1.358(3)Å | N4 | C9 | 1.320(3)Å |
| N5 | C14 | 1.356(3)Å | N4 | Fe1 | 2.1371(17)Å |
| N5 | Fe1 | 2.1344(17)Å | N5 | C20 | 1.323(3)Å |
| N6 | C20 | 1.393(3)Å | N6 | N7 | 1.379(2)Å |
| N7 | C22 | 1.293(3)Å | N6 | C21 | 1.480(3)Å |
| C1 | C2 | 1.399(3)Å | N7 | Fe1 | 2.270(2)Å |

| | | | | | |
|-----|-----|-----------|-----|-----|-----------|
| C2 | C3 | 1.381(3)Å | C1 | C22 | 1.497(3)Å |
| C3 | C4 | 1.389(4)Å | C6 | C7 | 1.506(3)Å |
| C4 | C5 | 1.394(3)Å | C10 | C11 | 1.367(3)Å |
| C5 | C6 | 1.496(3)Å | C11 | C12 | 1.429(3)Å |
| C9 | C10 | 1.425(3)Å | C12 | C13 | 1.399(3)Å |
| C12 | C17 | 1.431(3)Å | C13 | C14 | 1.432(3)Å |
| C14 | C15 | 1.398(3)Å | C15 | C16 | 1.437(3)Å |
| C15 | C18 | 1.423(3)Å | C16 | C17 | 1.366(3)Å |
| C18 | C19 | 1.369(3)Å | C22 | C23 | 1.505(3)Å |
| C19 | C20 | 1.428(3)Å | | | |

| | | | | | | | |
|----|-----|----|-----------|----|-----|----|-----------|
| O1 | Fe1 | N1 | 87.04(6)° | O1 | Fe1 | N2 | 86.50(6)° |
|----|-----|----|-----------|----|-----|----|-----------|

| | | | | | | | | |
|----|-----|-----|------------|--|----|-----|-----|------------|
| N1 | Fe1 | N2 | 72.66(7)° | | O1 | Fe1 | N4 | 92.21(6)° |
| N1 | Fe1 | N4 | 142.28(7)° | | N2 | Fe1 | N4 | 69.65(6)° |
| O1 | Fe1 | N5 | 93.43(6)° | | N4 | Fe1 | N5 | 74.88(7)° |
| O1 | Fe1 | N7 | 88.06(6)° | | N1 | Fe1 | N7 | 72.89(7)° |
| N5 | Fe1 | N7 | 69.98(6)° | | O1 | Fe1 | Cl1 | 174.27(4)° |
| N1 | Fe1 | Cl1 | 87.33(5)° | | N2 | Fe1 | Cl1 | 92.82(5)° |
| N4 | Fe1 | Cl1 | 92.89(5)° | | N5 | Fe1 | Cl1 | 90.43(5)° |
| N7 | Fe1 | Cl1 | 89.28(5)° | | | | | |

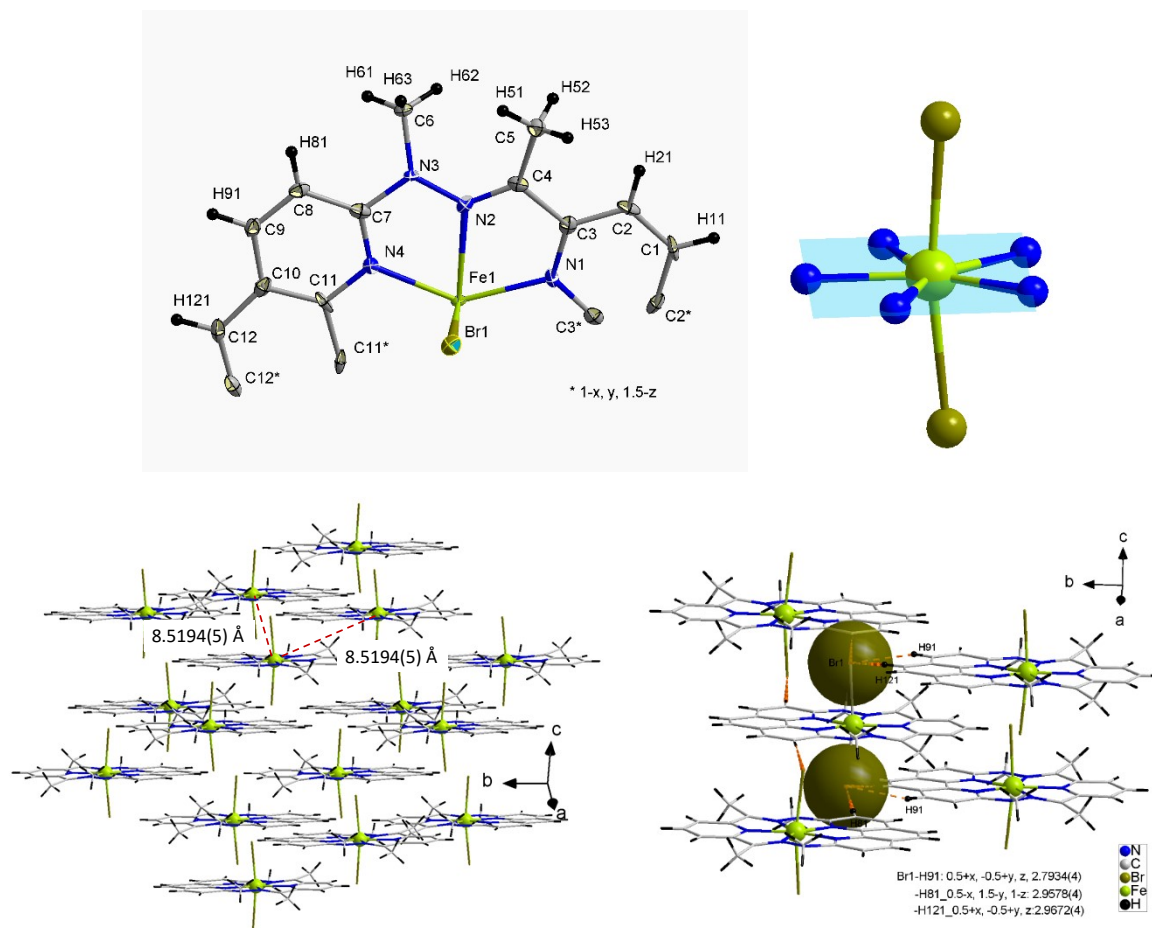
Figure S2. $[\text{FeL}^{\text{N5}}\text{Cl}_2] \cdot 5\text{H}_2\text{O}$, **2**: ORTEP plot of the asymmetric unit (50 % probability level) with numbering scheme, crystal packing, and selected inter-atomic distances and angles.



Selected interatomic distances (Å) and angles (°):

| | | | | | | |
|-----------------|-------|--------------------|-----------|--|-----|-----------|
| N2a | Fe1 | 2.4983(1) | | N3a | Fe1 | 2.3948(1) |
| N4a | Fe1 | 1.8158(1) | | Cl1 | Fe1 | 2.5390(4) |
| Fe1 | Fe1* | 8.4175(2) | | * = 0.5-x, 1.5-y, 1-z or 1.5-x, 1.5-y, 1-z | | |
| H...Cl contacts | | | | | | |
| Cl1 | H1o5 | (0.5+x, -0.5+y, z) | 2.3115(1) | (H ₂ O) | | |
| Cl1 | H1c9a | (0.5+x, 1.5-y, z) | 2.5316(1) | | | |
| Cl1 | H1c9a | (0.5+x, -0.5+y, z) | 2.8241(1) | | | |
| Cl1 | H1c6a | (0.5+x, 0.5+y, z) | 2.9134(1) | | | |

Figure S3. $[\text{FeL}^{\text{N5}}\text{Br}_2]$, **3**: ORTEP plot (50 % probability level) of the asymmetric unit with numbering scheme, first coordination sphere with plane (in blue) defined by the 5 N atoms in the equatorial sites, crystal packing, focus on the Br...H contacts (the van der Waals volume of the halogen atom is depicted), and selected inter-atomic distances.



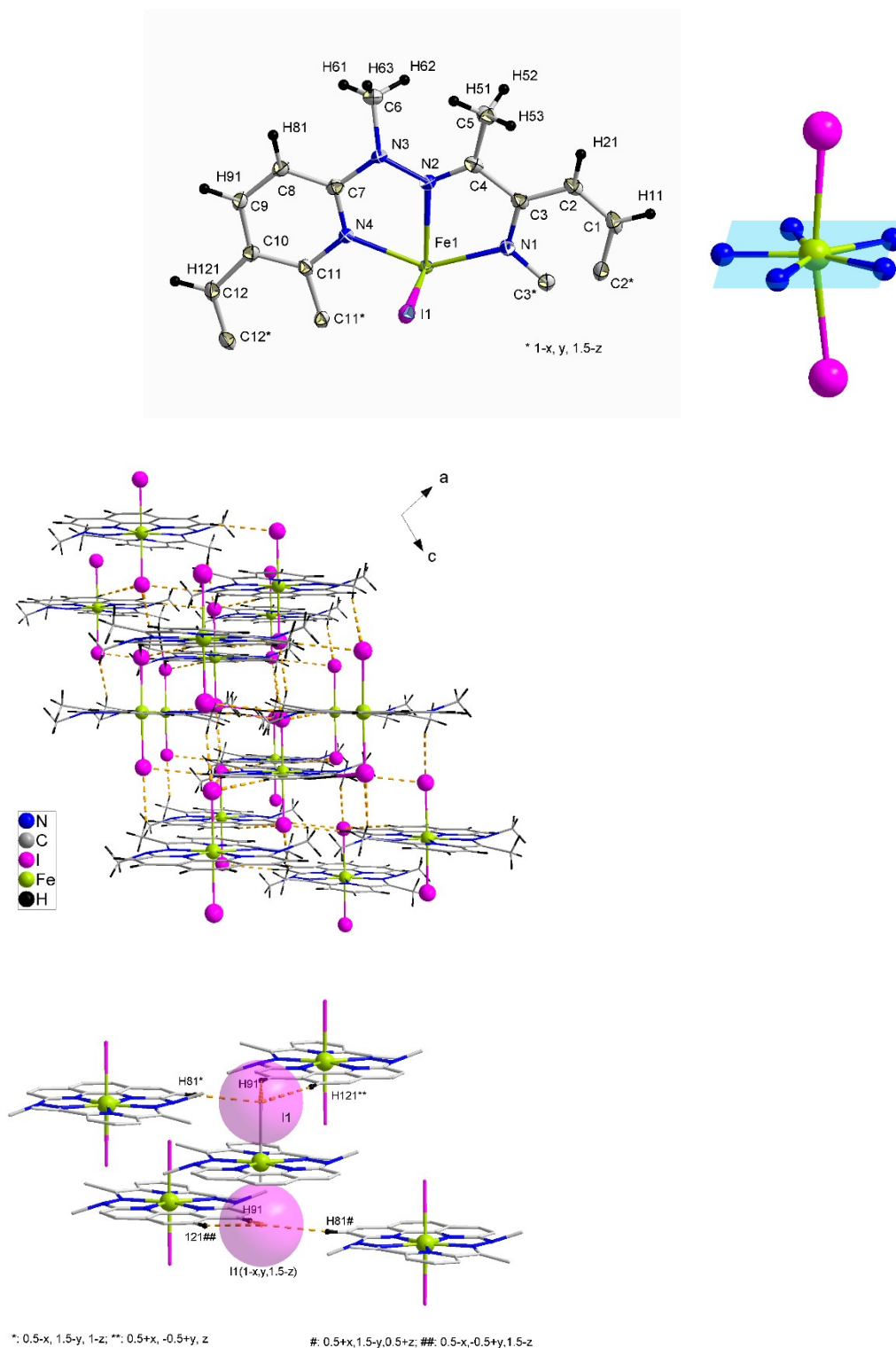
Selected interatomic distances (Å) and angles (°):

| | | | | | | |
|-----------------|------|---------------------|-----------|----|-----|----------|
| N1 | Fe1 | 2.128(5) | | N2 | Fe1 | 2.304(4) |
| N4 | Fe1 | 2.114(3) | | N2 | N3 | 1.364(5) |
| Br1 | Fe1 | 2.7106(5) | | | | |
| H...Br contacts | | | | | | |
| Br1 | H91 | (0.5+x, -0.5+y, z) | 2.8062(4) | | | |
| Br1 | H81 | (0.5-x, 1.5-y, 1-z) | 2.9585(4) | | | |
| Br1 | H121 | 0.5+x, -0.5+y, z | 3.0178(4) | | | |
| N1 | Fe1 | 2.128(4) | | N2 | Fe1 | 2.304(3) |
| N4 | Fe1 | 2.115(3) | | N2 | N3 | 1.362(4) |
| Br1 | Fe1 | 2.7108(4) | | | | |
| H...Br contacts | | | | | | |
| Br1 | H91 | (0.5+x, -0.5+y, z) | 2.7934(4) | | | |
| Br1 | H81 | (0.5-x, 1.5-y, 1-z) | 2.9578(4) | | | |
| Br1 | H121 | 0.5+x, -0.5+y, z | 2.9672(4) | | | |

| | | | | | | | | |
|----|-----|----|-----------|--|----|-----|----------|-----------|
| N1 | Fe1 | N2 | 71.99(9)° | | N1 | Fe1 | N2_6_656 | 71.99(9)° |
|----|-----|----|-----------|--|----|-----|----------|-----------|

| | | | | | | | | |
|-----|-----|----------|------------|--|-----------------|-----|----------|------------|
| N2 | Fe1 | N2 6_656 | 144.0(2)° | | N1 | Fe1 | N4 | 141.89(9)° |
| N2 | Fe1 | N4 | 69.9(1)° | | N2 | Fe1 | Br1 | 89.80(9)° |
| N1 | Fe1 | Br1 | 94.46(2)° | | N4 | Fe1 | Br1 | 85.7(1)° |
| N2* | Fe1 | Br1 | 92.96(9)° | | N1 | Fe1 | Br1* | 94.46(2)° |
| N4* | Fe1 | Br1 | 87.3(1)° | | N2* | Fe1 | Br1* | 89.80(9)° |
| N2 | Fe1 | Br1* | 92.96(9)° | | N4* | Fe1 | Br1* | 85.7(1)° |
| N4 | Fe1 | Br1* | 87.3(1)° | | Br1 | Fe1 | Br1* | 171.08(4)° |
| Br1 | Fe1 | Br1* | 171.08(4) | | * 1-x, y, 1.5-z | | | |
| N1 | Fe1 | N2 | 72.07(8)° | | N1 | Fe1 | N2 6_656 | 72.07(8)° |
| N2 | Fe1 | N2 6_656 | 144.2(1)° | | N1 | Fe1 | N4 | 141.93(8)° |
| N2 | Fe1 | N4 | 69.8(1)° | | N2 | Fe1 | Br1 | 89.84(8)° |
| N1 | Fe1 | Br1 | 94.47(2)° | | N4 | Fe1 | Br1 | 85.72(8)° |
| N2* | Fe1 | Br1 | 92.91(8)° | | N1 | Fe1 | Br1* | 94.47(2)° |
| N4* | Fe1 | Br1 | 87.24(8)° | | N2* | Fe1 | Br1* | 89.84(8)° |
| N2 | Fe1 | Br1* | 92.91(8)° | | N4* | Fe1 | Br1* | 85.72(8)° |
| N4 | Fe1 | Br1* | 87.24(8)° | | Br1 | Fe1 | Br1* | 171.05(3)° |
| Br1 | Fe1 | Br1* | 171.05(3)° | | * 1-x, y, 1.5-z | | | |

Figure S4. $[\text{FeL}^{\text{N5}}\text{I}_2]$, **4**: ORTEP plot (50 % probability level) of the asymmetric unit with numbering scheme, first coordination sphere with plane (in blue) defined by the 5 N atoms in the equatorial sites, crystal packing with I---H contacts (dotted lines), detail of the I---H bonds (the van der Waals volume of the halogen atom is depicted), and selected inter-atomic distances.



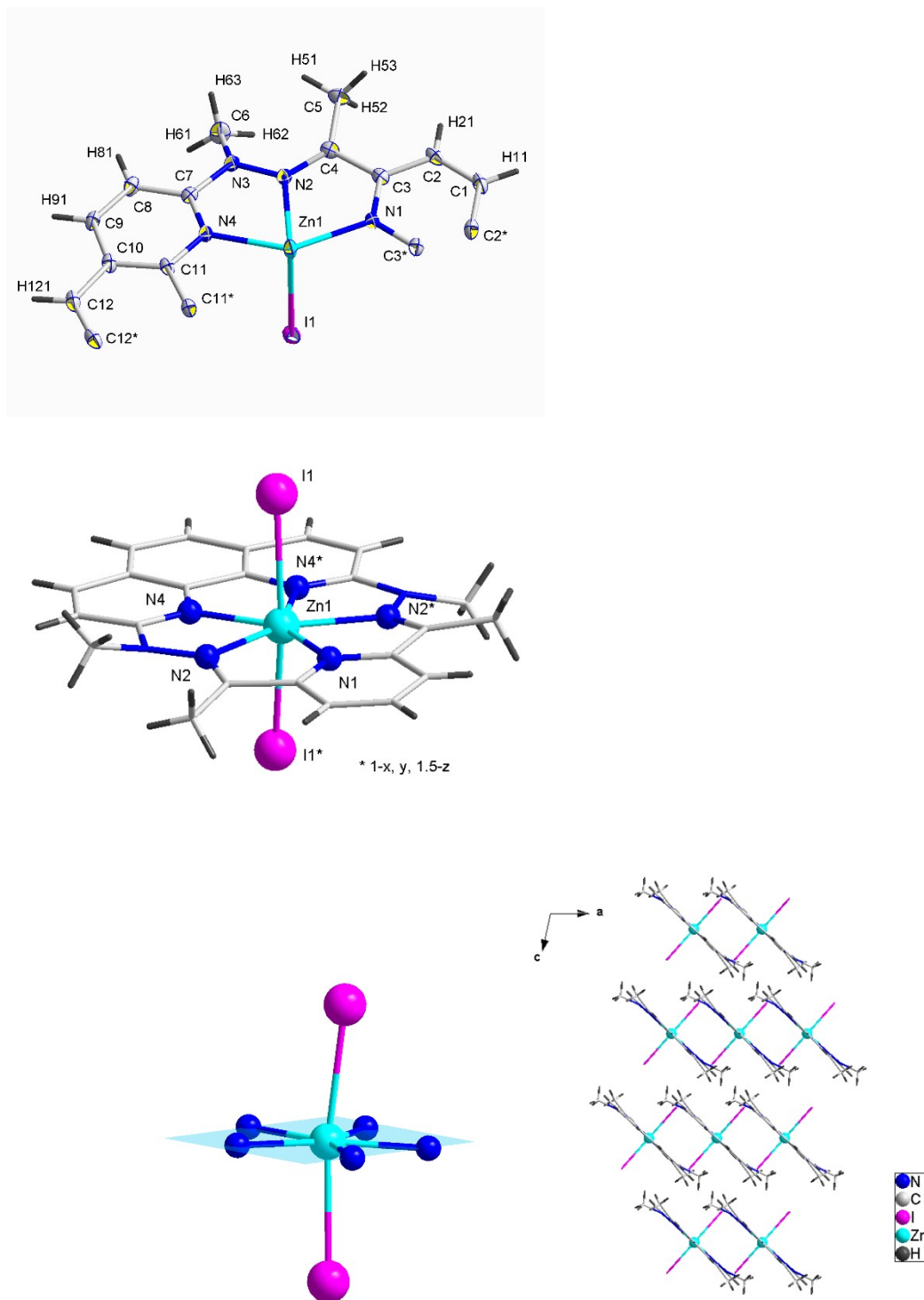
Selected interatomic distances (Å) and angles (°):

| | | | | | | |
|----------------|------|-------------------|-----------|----|-----|-----------|
| N1 | Fe1 | 2.105(3) | | N2 | N3 | 1.372(3) |
| N3 | C6 | 1.474(3) | | N2 | Fe1 | 2.280(2) |
| N4 | Fe1 | 2.123(2) | | I1 | Fe1 | 0.9231(1) |
| H...X contacts | | | | | | |
| I1 | H121 | 0.5+x, -0.5+y, z | 3.0592(2) | | | |
| I1 | H81 | 0.5-x, 1.5-y, 1-z | 3.1236(2) | | | |
| I1 | H53 | 1-x, 1-y, 1-z | 3.1567(2) | | | |
| I1 | H91 | 0.5+x, -0.5+y, z | 3.1730(2) | | | |

| | | | | | | | | |
|-----|-----|-----|-------------|--|-----|-----|-----|------------|
| N1 | Fe1 | N2 | 72.46(5)° | | N1 | Fe1 | N2* | 72.46(5)° |
| N2 | Fe1 | N4 | 69.83(7)° | | N1 | Fe1 | N4 | 142.29(5)° |
| N1 | Fe1 | I1 | 94.723(9)° | | N4 | Fe1 | N4* | 75.43(10)° |
| N2* | Fe1 | I1 | 92.09(5)° | | N2 | Fe1 | I1 | 90.75(5)° |
| N4* | Fe1 | I1 | 86.94(5)° | | N4 | Fe1 | I1 | 85.59(5)° |
| N2 | Fe1 | I1* | 92.09(5)° | | N1 | Fe1 | I1* | 94.723(9)° |
| N4 | Fe1 | I1* | 86.94(5)° | | N2* | Fe1 | I1* | 90.75(5)° |
| I1 | Fe1 | I1* | 70.554(18)° | | N4* | Fe1 | I1* | 85.59(5)° |

* 1-x, y, 1.5-z

Figure S5. $[\text{ZnL}^{\text{N5}}\text{I}_2]$: asymmetric unit (ORTEP plot at 50 % probability level) with numbering scheme, molecular complex, first coordination sphere with plane (in blue) defined by the 5 N atoms in the equatorial sites, crystal packing, and selected inter-atomic distances.



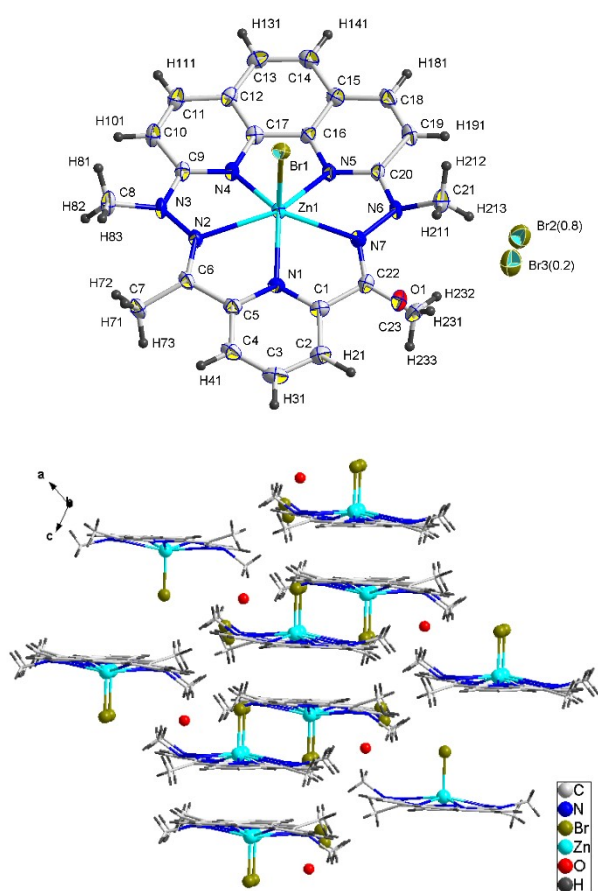
Selected interatomic distances (Å) and angles (°):

| | | | | | | |
|----|-----|----------|--|----|-----|----------|
| N1 | Zn1 | 2.096(4) | | N2 | N3 | 1.363(4) |
| N2 | C4 | 1.285(5) | | N2 | Zn1 | 2.317(3) |

| | | | | | | |
|----|-----|-----------|--|----|----|----------|
| N4 | Zn1 | 2.116(3) | | N3 | C7 | 1.395(4) |
| I1 | Zn1 | 2.9551(2) | | | | |

| | | | | | | | | |
|-----|-----|-----|-------------|--|-----|-----|-----|-------------------|
| N1 | Zn1 | N2 | 72.50(7)° | | N2 | Zn1 | I1 | 92.08(7)° |
| N2 | Zn1 | N4 | 69.35(11)° | | N4 | Zn1 | I1 | 86.92(8)° |
| N1 | Zn1 | I1 | 94.688(12)° | | N1 | Zn1 | I1* | 94.688(12)° |
| N2* | Zn1 | I1 | 90.74(7)° | | N2* | Zn1 | I1* | 92.08(7)° |
| N4* | Zn1 | I1 | 85.71(8)° | | N4* | Zn1 | I1* | 86.92(8)° |
| N2 | Zn1 | I1* | 90.74(7)° | | I1 | Zn1 | I1* | 170.62(2)° |
| N4 | Zn1 | I1* | 85.71(8)° | | | | | * = 1-x, y, 1.5-z |

Figure S6. [ZnL^{N5}Br]Br·0.5H₂O : ORTEP plot (50 % probability level) with numbering scheme, crystal packing, and selected inter-atomic distances.



Selected interatomic distances (Å) and angles (°):

| | | | | | | |
|-----|-----|-----------|--|----|-----|----------|
| N2 | N3 | 1.370(6) | | N1 | Zn1 | 2.134(4) |
| N4 | Zn1 | 2.158(4) | | N2 | Zn1 | 2.350(4) |
| N6 | N7 | 1.379(6) | | N5 | Zn1 | 2.172(4) |
| Br1 | Zn1 | 2.4267(8) | | N7 | Zn1 | 2.270(4) |

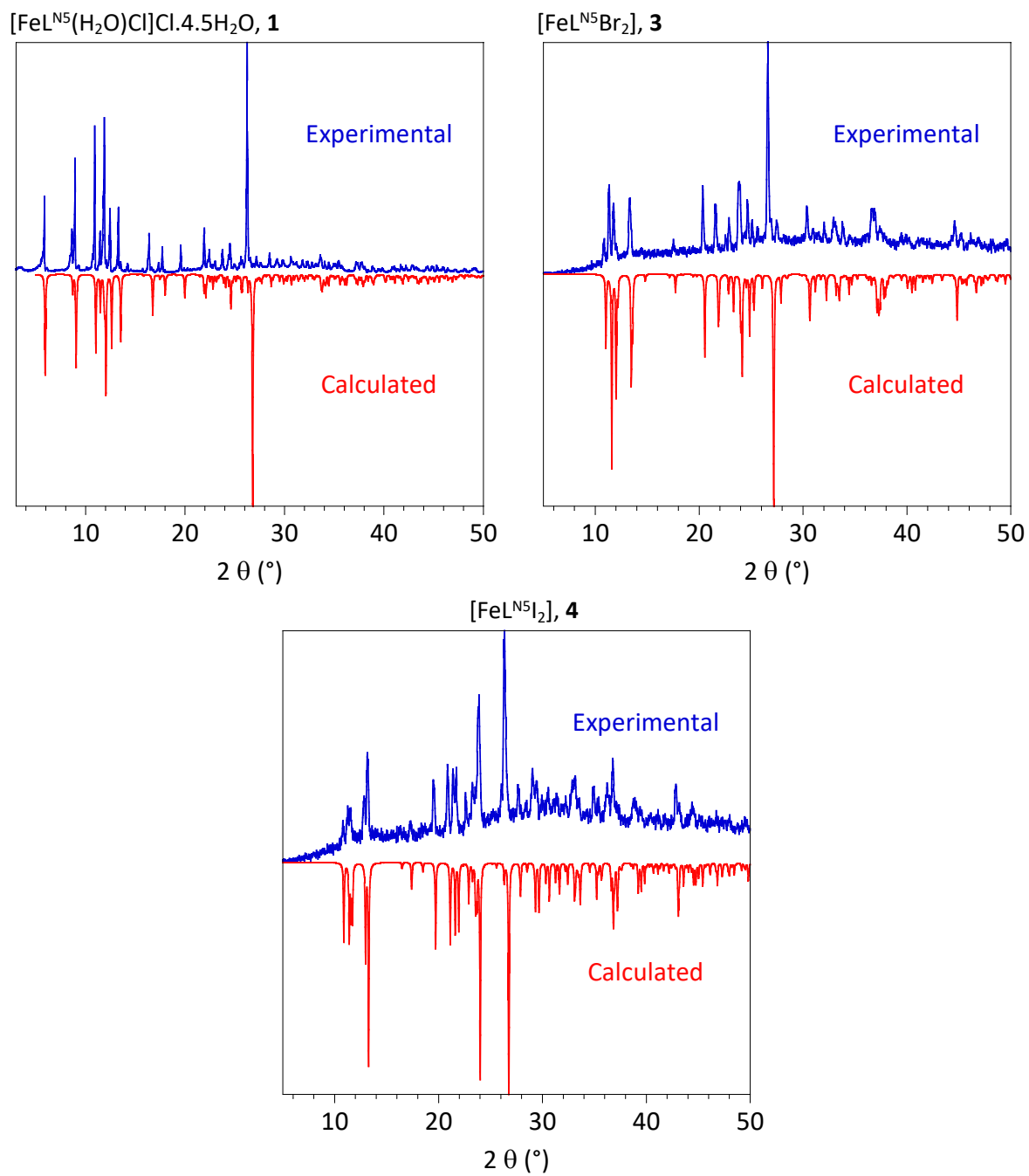
| | | | | | | | | |
|----|-----|----|------------|--|----|-----|----|------------|
| N1 | Zn1 | N2 | 70.56(16)° | | N4 | Zn1 | N5 | 74.02(16)° |
|----|-----|----|------------|--|----|-----|----|------------|

| | | | | | | | | |
|----|-----|-----|-------------|--|----|-----|-----|-------------|
| N2 | Zn1 | N4 | 67.76(15)° | | N5 | Zn1 | N7 | 67.97(15)° |
| N1 | Zn1 | N7 | 71.92(16)° | | N2 | Zn1 | Br1 | 102.17(10)° |
| N1 | Zn1 | Br1 | 110.36(12)° | | N5 | Zn1 | Br1 | 97.64(11)° |
| N4 | Zn1 | Br1 | 100.12(11)° | | N7 | Zn1 | Br1 | 97.72(11)° |

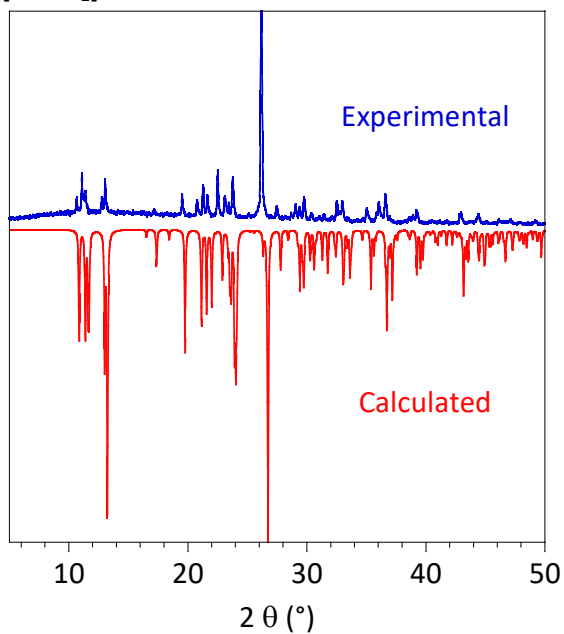
Table S2. Results of SHAPE analysis⁸ of the actual coordination polyhedral⁹ and equatorial plane deformations for **1-4**, and **ZnL^{N5}I₂**.

| <i>CShM</i> parameter | Reference geometry | 1 | 2 (Fe1/Fe2) | 3 | 4 | ZnL ^{N5} I ₂ |
|----------------------------|----------------------|-------|-------------|-------|-------|----------------------------------|
| for [FeL ^{N5}] | pentagonal | 0.162 | 0.113/0.161 | 0.188 | 0.352 | 0.255 |
| for [FeL ^{N5} XY] | pentagonal bipyramid | 0.499 | 1.002/1.060 | 1.326 | 2.214 | 2.361 |

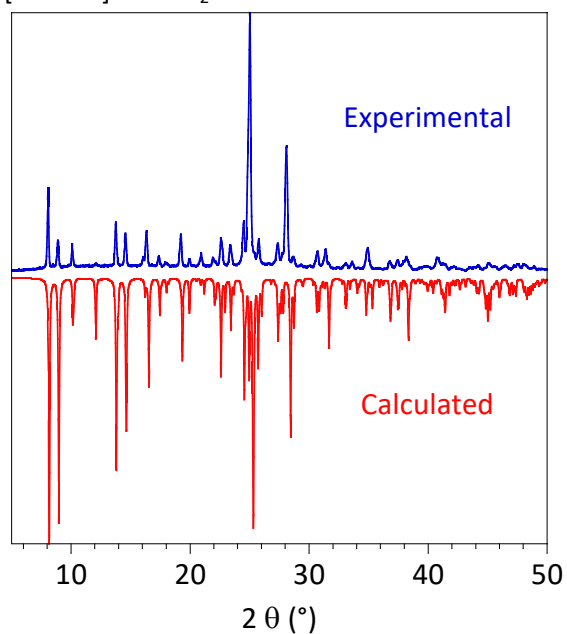
Figure S7. PXRD for **1**, **3-5**, $[\text{ZnL}^{\text{N5}}\text{I}_2]$, and $[\text{ZnL}^{\text{N5}}\text{Br}]\text{Br}\cdot 0.5\text{H}_2\text{O}$.



[ZnL^{N5}I₂]



[ZnL^{N5}Br]Br·0.5H₂O



[Fe_{0.12}Zn_{0.88}L^{N5}I₂], 5

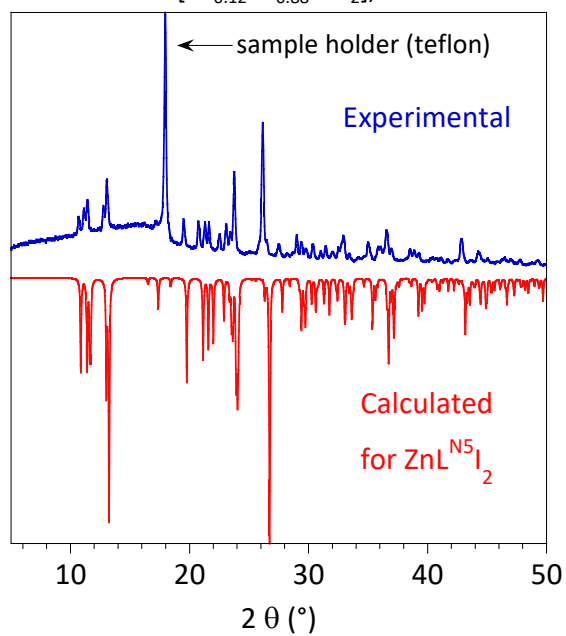
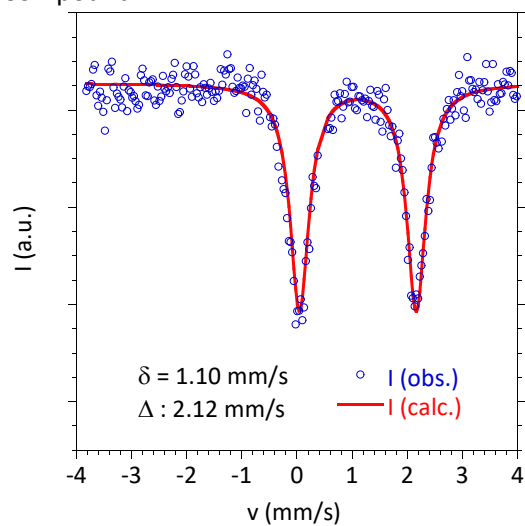
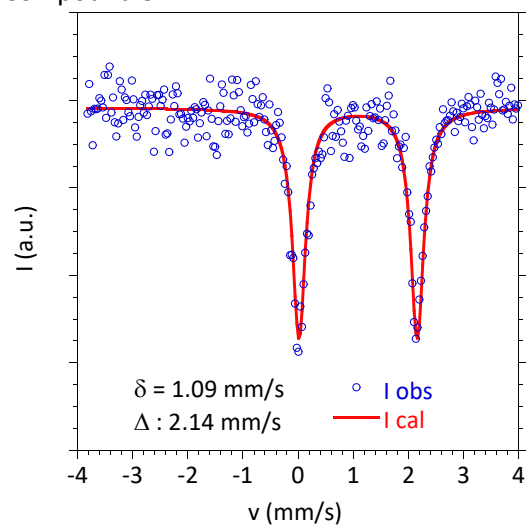


Figure S8. Mössbauer spectra for **1**, **3**, and **4**: Experimental (\circ) recorded at 80 K and calculated ($—$), with chemical shift (δ) and quadrupole splitting (Δ).

Compound 1



Compound 3



Compound 4

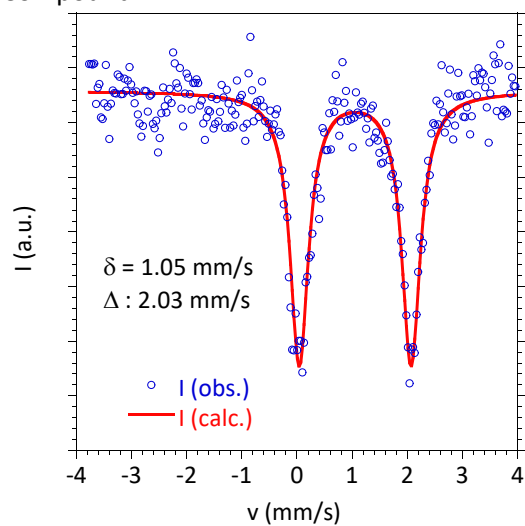
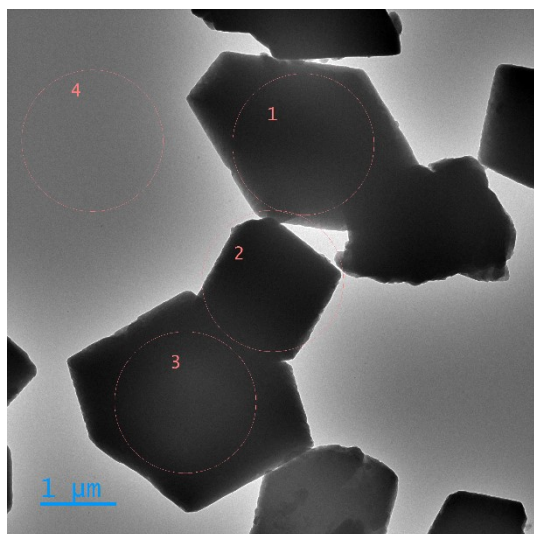
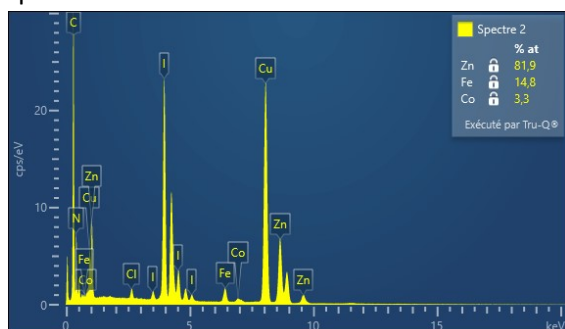


Figure S9. Energy dispersive X-ray (EDX) analysis for $[\text{Fe}_{0.12}\text{Zn}_{0.88}\text{L}^{\text{N5}}\text{I}_2]$, **5**.

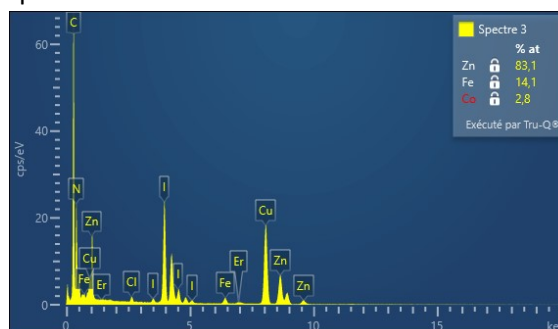


Relative Zn/Fe atomic compositions for several individual crystals (the Cu signals come from the Cu-grid used for the analysis, the trace impurities of Co and Fe were also from the grid; see spot 4)

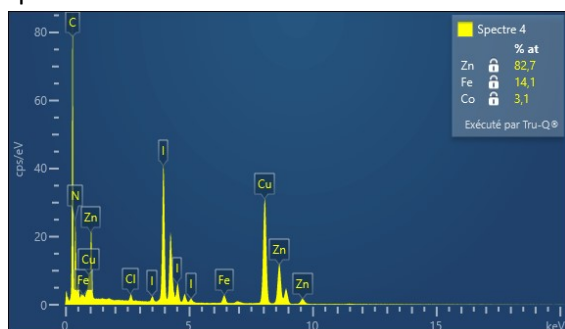
Spot 1



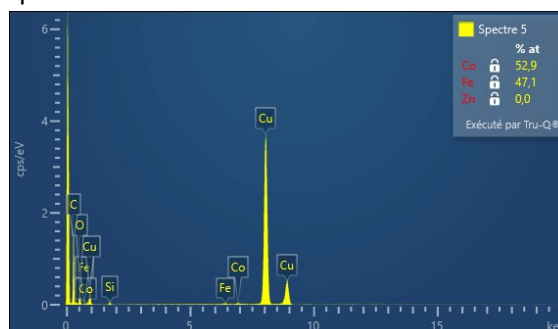
Spot 2



Spot 3



Spot 4



From these data, a relative atom content (at%) of 82.4 and 11.6 is obtained respectively for Zn and Fe. These correspond to a molar ratio for these ions of respectively 88 and 12 mol% leading to the formula $[\text{Fe}_{0.12}\text{Zn}_{0.88}\text{L}^{\text{N5}}\text{I}_2]$ for **5**.

Figure S10. M versus H at 2-8 K for **1**, **3-5**. In (b) and (d) the experimental data are compared to the calculated magnetizations (solid lines); for **5** the calculated behavior has been scaled by 0.94. In (c) solid lines are just eye-guides. (e) M versus H loop for **5** between 50 and -50 kOe recorded with field scanning speed of about 40 Oe/s.

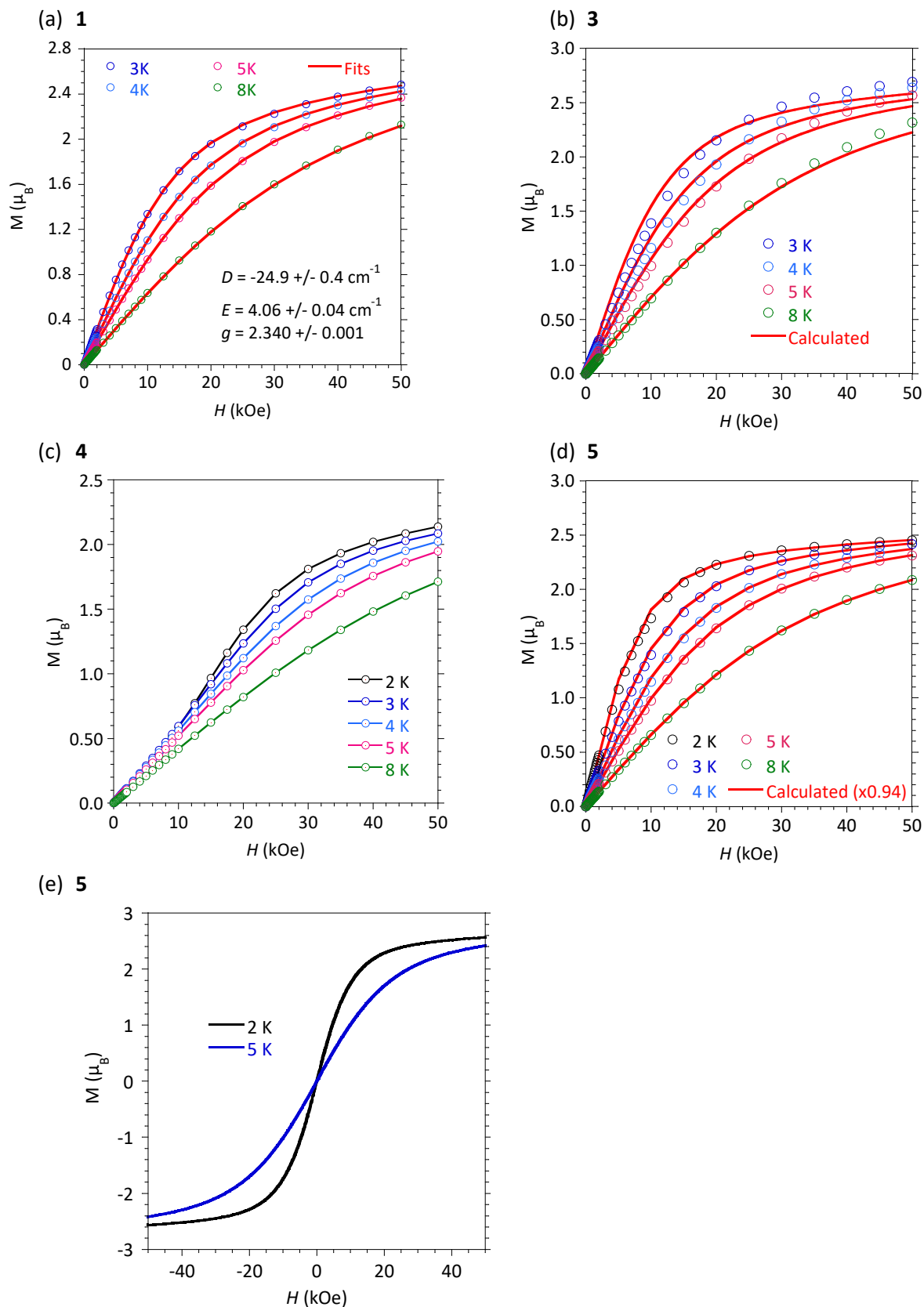


Figure S11. AC magnetic susceptibility for **1**.

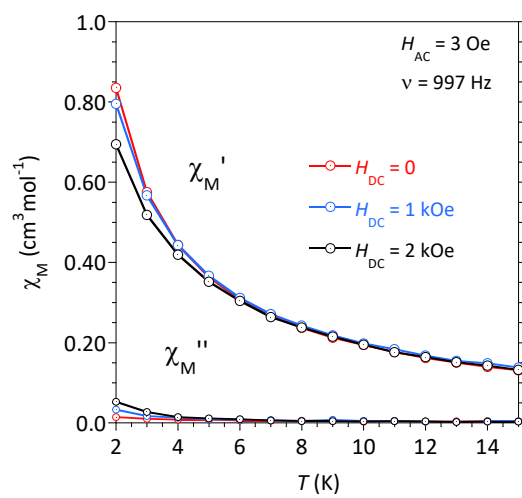
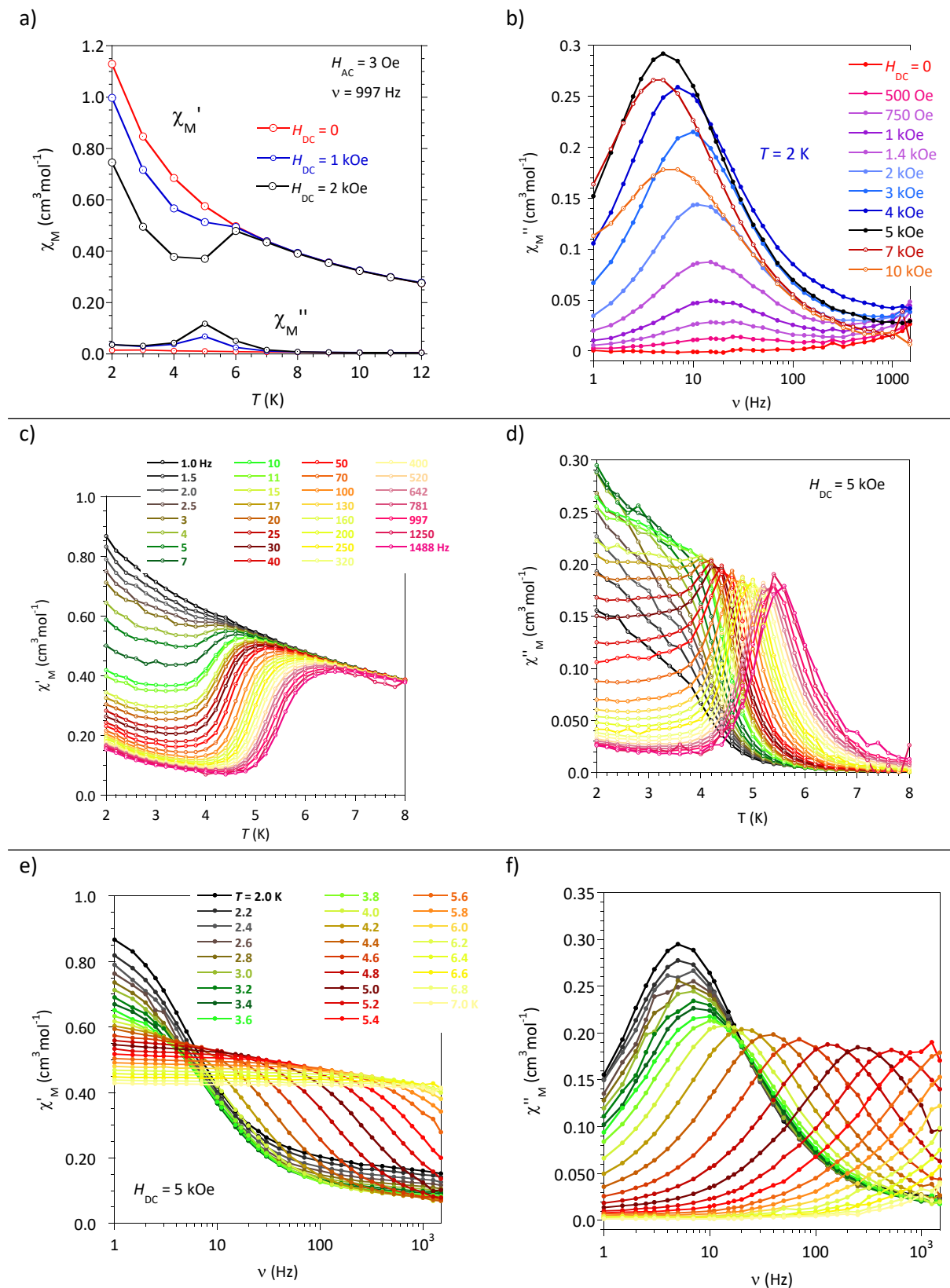


Figure S12. AC magnetic susceptibility for **3**: a) χ_M' and χ_M'' versus T without applied field and with $H_{DC} = 1$ kOe and 2 kOe; b) frequency dependence of χ_M'' at 2 K for different applied DC fields; c-d) χ_M' and χ_M'' versus T for frequencies between 1 and 1500 Hz ($H_{DC} = 5$ kOe); e-f) χ_M' and χ_M'' versus ν for different T ($H_{DC} = 5$ kOe); g) Cole-Cole plot; h) best fit of a generalized Debye model (solid red lines) to χ_M'' versus ν for different T (fit parameters are in Table S3.)



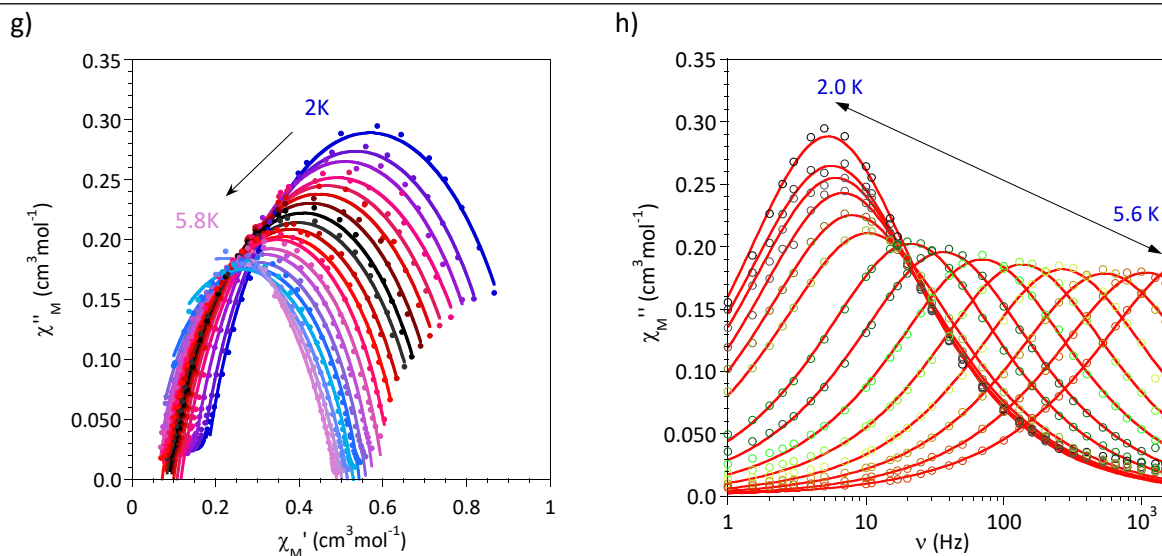
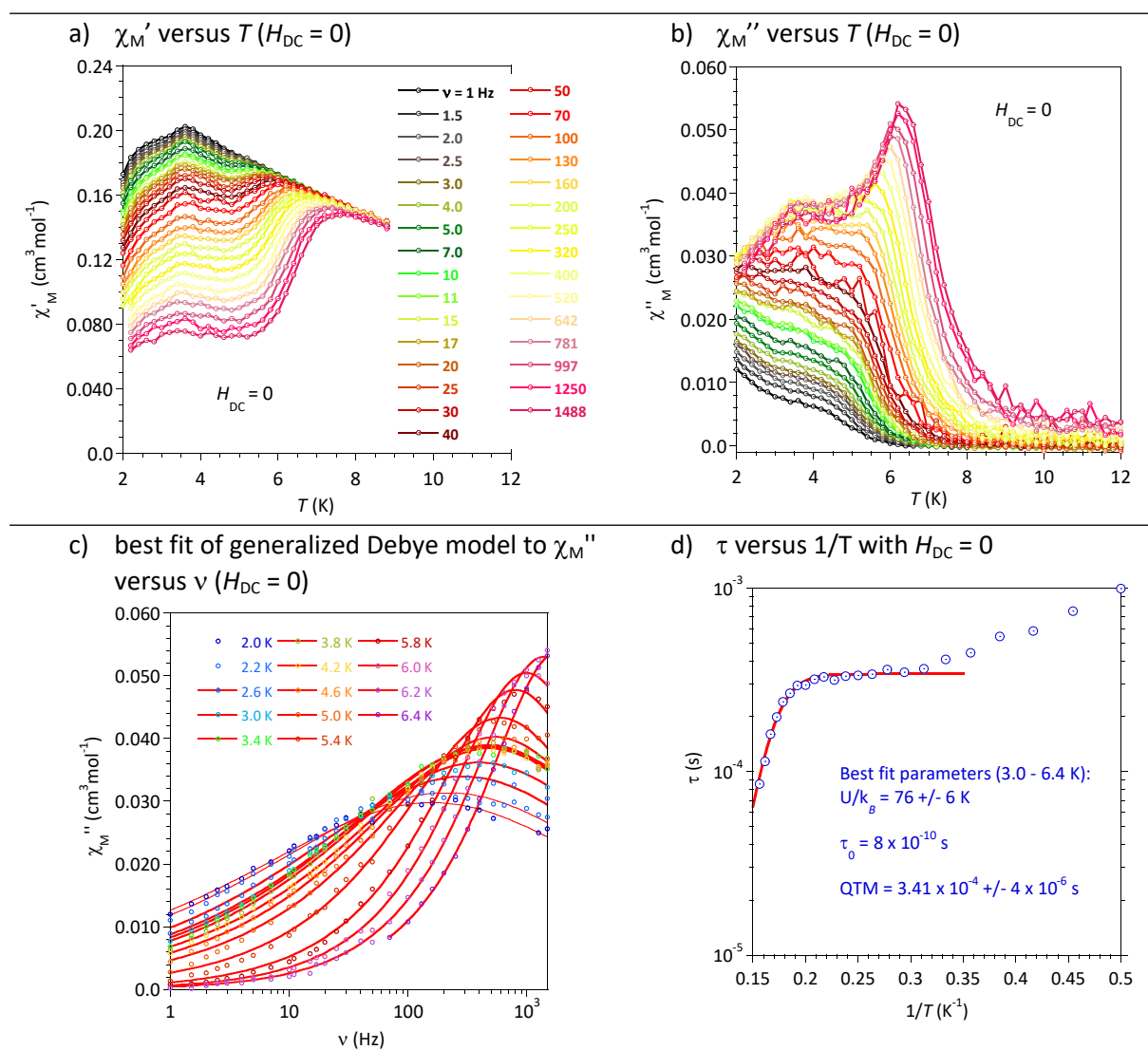
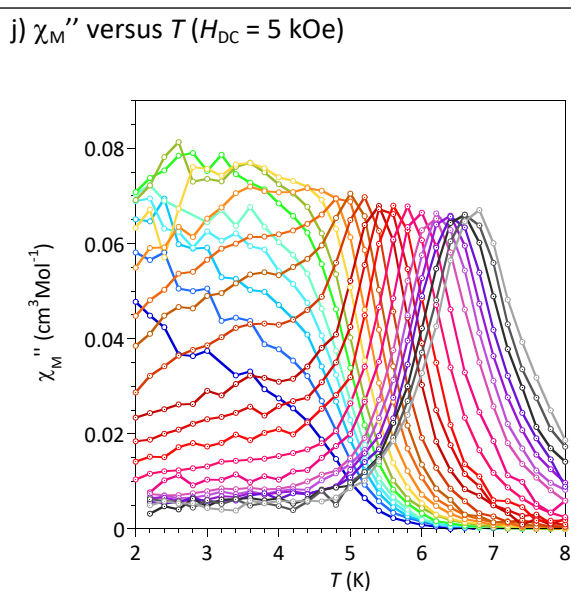
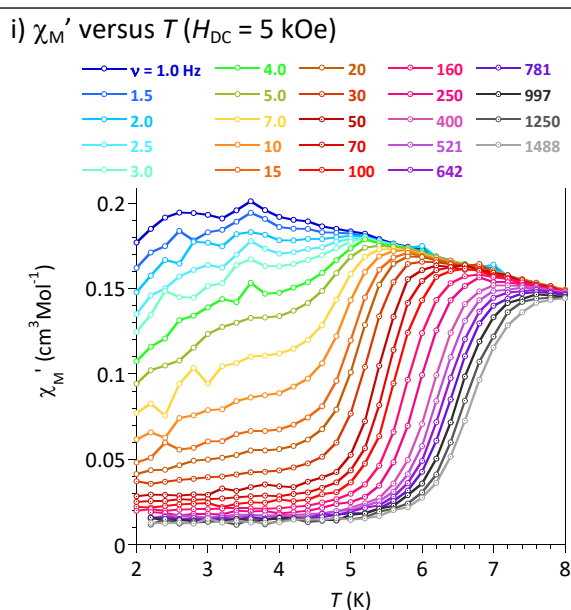
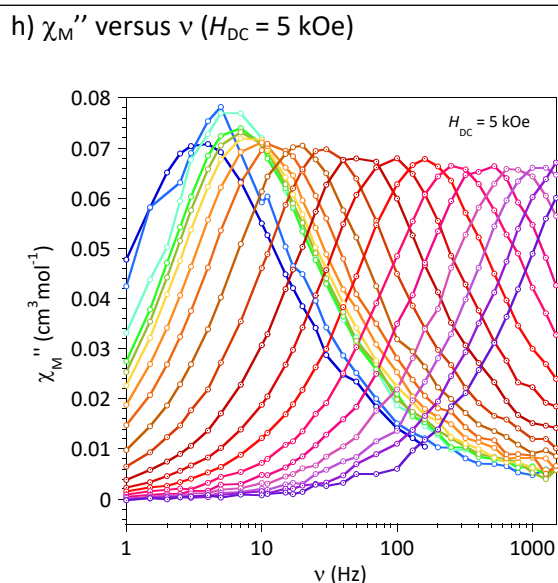
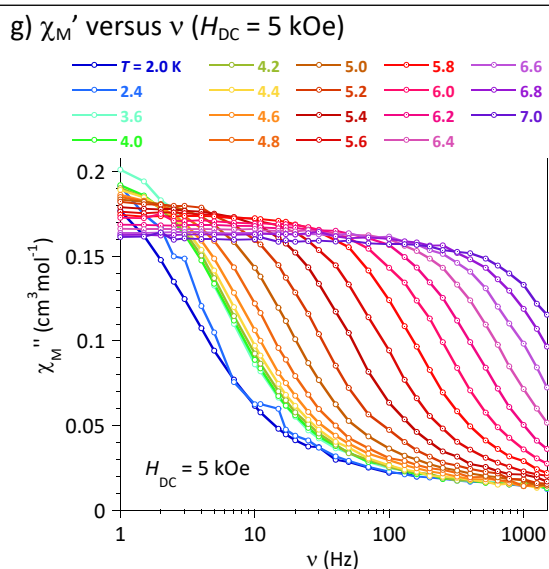
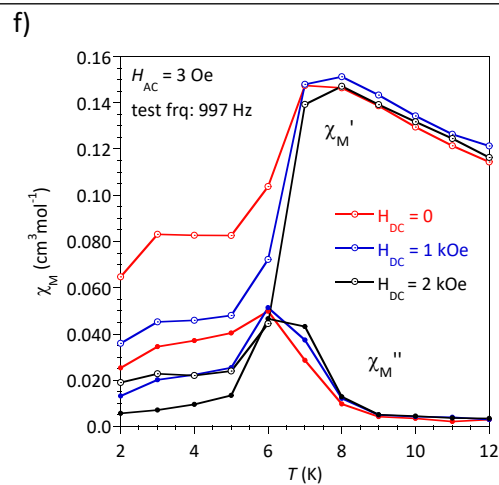
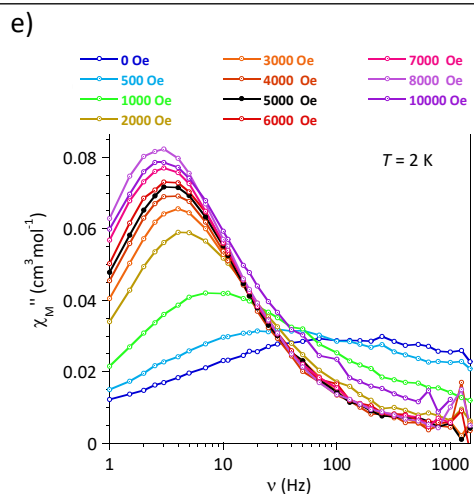


Table S3. Best-fit parameters of the analyses of χ_M'' versus ν ($H_{DC} = 5$ kOe) by a generalized Debye model¹⁰ for **3** (Figure S12h).

| T (K) | χ_t | χ_s | τ (s) | α | R |
|-------|----------|----------|-------------|----------|---------|
| 2.0 | 2.448 | 1.652 | 0.029723 | 0.20494 | 0.99607 |
| 2.2 | 2.4352 | 1.6648 | 0.029101 | 0.22053 | 0.99693 |
| 2.4 | 2.4277 | 1.6723 | 0.028133 | 0.22534 | 0.99779 |
| 2.6 | 2.4134 | 1.6866 | 0.026264 | 0.2247 | 0.99786 |
| 2.8 | 2.402 | 1.698 | 0.024784 | 0.21726 | 0.9981 |
| 3.0 | 2.3919 | 1.7081 | 0.023334 | 0.21723 | 0.99823 |
| 3.2 | 2.3809 | 1.7191 | 0.021482 | 0.22259 | 0.99852 |
| 3.4 | 2.3692 | 1.7308 | 0.01968 | 0.22142 | 0.99872 |
| 3.6 | 2.3629 | 1.7371 | 0.018074 | 0.2322 | 0.99859 |
| 3.8 | 2.3505 | 1.7495 | 0.015265 | 0.22458 | 0.99891 |
| 4.0 | 2.3378 | 1.7622 | 0.011396 | 0.20868 | 0.9991 |
| 4.2 | 2.3274 | 1.7726 | 0.0075324 | 0.19969 | 0.99881 |
| 4.4 | 2.318 | 1.782 | 0.0043812 | 0.20015 | 0.99816 |
| 4.6 | 2.31 | 1.79 | 0.0022893 | 0.20013 | 0.99783 |
| 4.8 | 2.3033 | 1.7967 | 0.0011745 | 0.19715 | 0.99766 |
| 5.0 | 2.2978 | 1.8022 | 0.00060403 | 0.19649 | 0.99713 |
| 5.2 | 2.3036 | 1.7964 | 0.00029382 | 0.22276 | 0.99867 |
| 5.4 | 2.3224 | 1.7776 | 0.00013165 | 0.2496 | 0.99854 |
| 5.6 | 2.3644 | 1.7356 | 0.000053436 | 0.28469 | 0.99936 |

Figure S13. AC magnetic susceptibility for **4**: a-b) χ_M' and χ_M'' versus T in zero field for frequencies between 1 and 1500 Hz; c) best fit of a generalized Debye model (solid red lines) to χ_M'' versus ν ($H_{DC} = 0$) for different T (fit parameters are in Table S4.) d) τ versus $1/T$ in zero field, with best-fit parameters associated with Eq. 6 (main text); e) χ_M' and χ_M'' versus T without applied field and with $H_{DC} = 1$ kOe and 2 kOe; f) frequency dependence of χ_M'' at 2 K for different applied DC fields; g-h) frequency dependence of χ_M' and χ_M'' versus T for $H_{DC} = 5$ kOe; i-j) temperature dependence of χ_M' and χ_M'' versus ν for $H_{DC} = 5$ kOe; k) best fit of a generalized Debye model (solid red lines) to χ_M'' versus ν ($H_{DC} = 5$ kOe) for different T (the fit parameters are in Table S4.) ; l) τ versus $1/T$ with $H_{DC} = 5$ kOe with best-fit parameters associated with Eq. 6 (main text).





k) best fit of generalized Debye model (solid

l) τ versus $1/T$ with $H_{DC} = 5$ kOe

red lines) to χ_M'' versus ν ($H_{DC} = 5$ kOe)

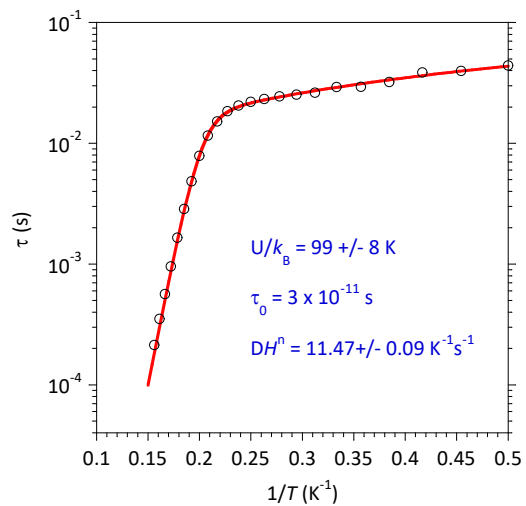
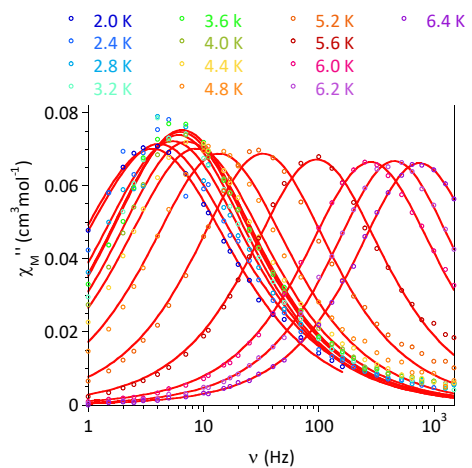


Table S4. Best-fit parameters of the analyses of χ_M'' versus ν by a generalized Debye model¹⁰ for **4** (Figures S13c and k): a) no applied static field, b) with $H_{DC} = 5$ kOe

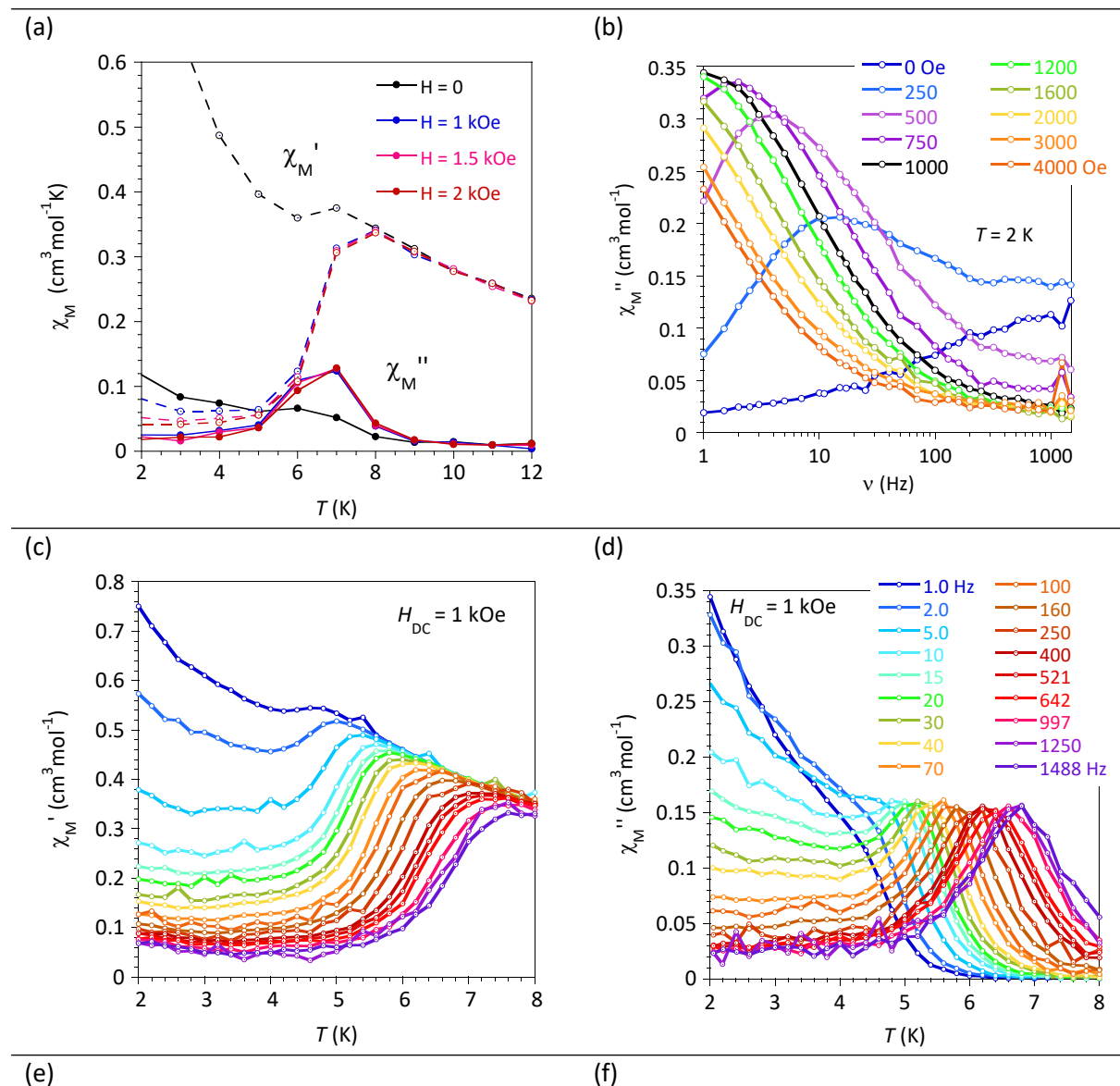
a) $H_{DC} = 0$

| T (K) | χ_t | χ^s | τ (s) | α | R |
|-------|----------|----------|------------|----------|---------|
| 2.0 | 2.5304 | 2.4696 | 0.00099551 | 0.70172 | 0.99419 |
| 2.2 | 3.032 | 2.968 | 0.00075084 | 0.69385 | 0.99408 |
| 2.4 | 3.0336 | 2.9664 | 0.00058511 | 0.68128 | 0.99724 |
| 2.6 | 3.0346 | 2.9654 | 0.00054708 | 0.66179 | 0.99773 |
| 2.8 | 3.5358 | 3.4642 | 0.00044553 | 0.65798 | 0.99764 |
| 3.0 | 4.0368 | 3.9632 | 0.00040854 | 0.64661 | 0.99817 |
| 3.2 | 4.0382 | 3.9618 | 0.00036374 | 0.64365 | 0.99818 |
| 3.4 | 4.0393 | 3.9607 | 0.00034949 | 0.63539 | 0.99841 |
| 3.6 | 4.0395 | 3.9605 | 0.00036044 | 0.62777 | 0.99805 |
| 3.8 | 4.0395 | 3.9605 | 0.00034017 | 0.62809 | 0.99735 |
| 4.0 | 4.0397 | 3.9603 | 0.00033538 | 0.61397 | 0.99894 |
| 4.2 | 4.0391 | 3.9609 | 0.0003315 | 0.60679 | 0.99898 |
| 4.4 | 4.0396 | 3.9604 | 0.00031553 | 0.59869 | 0.99798 |
| 4.6 | 4.0397 | 3.9603 | 0.00032893 | 0.57994 | 0.99904 |
| 4.8 | 4.0402 | 3.9598 | 0.00031964 | 0.56482 | 0.99878 |
| 5.0 | 4.0409 | 3.9591 | 0.00029711 | 0.54483 | 0.99796 |
| 5.2 | 4.0418 | 3.9582 | 0.00029581 | 0.52205 | 0.99818 |
| 5.4 | 4.0439 | 3.9561 | 0.00026726 | 0.45427 | 0.99833 |
| 5.6 | 4.046 | 3.954 | 0.00024 | 0.39713 | 0.99843 |
| 5.8 | 4.0482 | 3.9518 | 0.00019832 | 0.3378 | 0.99917 |
| 6.0 | 4.0509 | 3.9491 | 0.00015992 | 0.27072 | 0.9995 |
| 6.2 | 4.0534 | 3.9466 | 0.0001139 | 0.24702 | 0.99963 |
| 6.4 | 4.0542 | 3.9458 | 8.5872e-5 | 0.21962 | 0.99975 |

b) $H_{DC} = 5$ kOe

| T (K) | χ_t | χ^s | τ (s) | α | R |
|-------|----------|----------|------------|----------|---------|
| 2.0 | 2.1483 | 1.9517 | 0.04403 | 0.21101 | 0.99852 |
| 2.2 | 2.1508 | 1.9492 | 0.03967 | 0.21122 | 0.99743 |
| 2.4 | 2.1536 | 1.9464 | 0.03862 | 0.2345 | 0.99135 |
| 2.6 | 2.149 | 1.951 | 0.03213 | 0.1771 | 0.99237 |
| 2.8 | 2.1475 | 1.9525 | 0.02934 | 0.18785 | 0.99264 |
| 3.0 | 2.1508 | 1.9492 | 0.02926 | 0.20251 | 0.99718 |
| 3.2 | 2.1467 | 1.9533 | 0.02626 | 0.1686 | 0.99418 |
| 3.4 | 2.1494 | 1.9506 | 0.02521 | 0.17866 | 0.99642 |
| 3.6 | 2.1499 | 1.9501 | 0.02445 | 0.17739 | 0.99641 |
| 3.8 | 2.1472 | 1.9528 | 0.02329 | 0.1712 | 0.99562 |
| 4.0 | 2.1447 | 1.9553 | 0.02207 | 0.17099 | 0.99607 |
| 4.2 | 2.1432 | 1.9568 | 0.02052 | 0.16762 | 0.99593 |
| 4.4 | 2.1422 | 1.9578 | 0.01843 | 0.17084 | 0.99519 |
| 4.6 | 2.1401 | 1.9599 | 0.01514 | 0.16961 | 0.99318 |
| 4.8 | 2.1375 | 1.9625 | 0.01158 | 0.15084 | 0.99382 |
| 5.0 | 2.1355 | 1.9645 | 0.00785 | 0.13512 | 0.9929 |
| 5.2 | 2.1342 | 1.9658 | 0.00485 | 0.12738 | 0.9939 |
| 5.4 | 2.1325 | 1.9675 | 0.00286 | 0.12167 | 0.99565 |
| 5.6 | 2.1309 | 1.9691 | 0.00165 | 0.11736 | 0.99697 |
| 5.8 | 2.1305 | 1.9695 | 0.000954 | 0.11253 | 0.99909 |
| 6.0 | 2.1294 | 1.9706 | 0.000564 | 0.11212 | 0.99959 |
| 6.2 | 2.1269 | 1.9731 | 0.000351 | 0.08913 | 0.9998 |
| 6.4 | 2.1269 | 1.9731 | 0.000213 | 0.09488 | 0.99985 |

Figure S14. AC magnetic susceptibility for **5**: a) χ_M' and χ_M'' versus T for $H_{DC} = 0, 1 \text{ kOe}, 1.5 \text{ kOe},$ and 2 kOe ; b) frequency dependence of χ_M'' at 2 K for different applied DC fields; c-d) frequency dependence of χ_M' and χ_M'' versus T for $H_{DC} = 1 \text{ kOe}$; e-f) temperature dependence of χ_M' and χ_M'' versus ν for $H_{DC} = 1 \text{ kOe}$, the solid red lines in S14f are the best fits of generalized Debye model (the fit parameters are in Table S54.) .



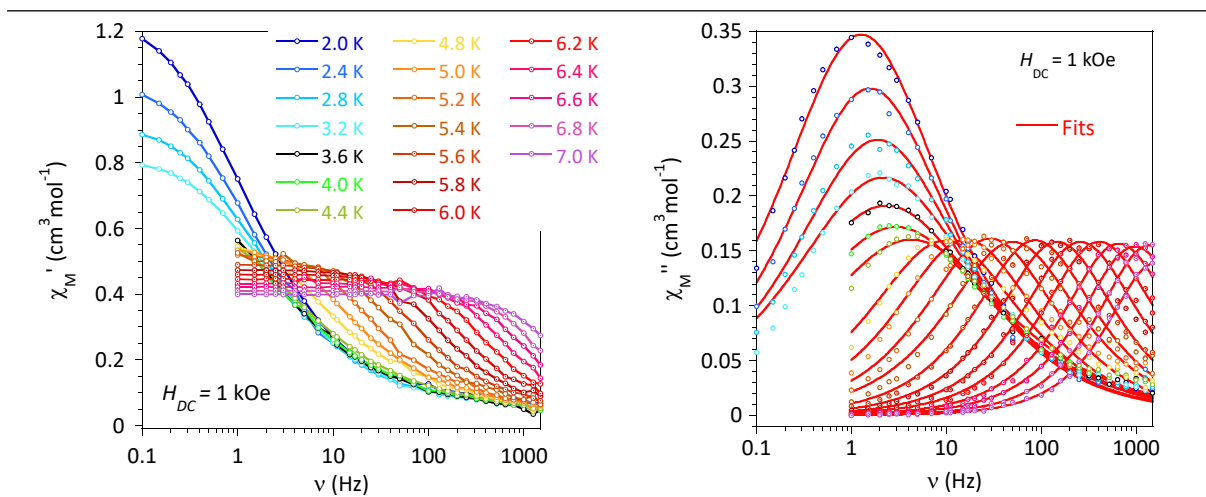


Table S5. Best-fit parameters of the analyses of χ_M'' versus ν (Figure S14f,) by a generalized Debye model¹⁰ for **5** ($H_{DC} = 1$ kOe).

| T (K) | χ_t | χ_s | Tau (s) | Alpha | R |
|-------|----------|----------|------------|---------|---------|
| 2.0 | 0.90134 | 0.19866 | 0.12518 | 0.44000 | 0.99772 |
| 2.2 | 0.86848 | 0.23152 | 0.11583 | 0.46000 | 0.99889 |
| 2.4 | 0.85159 | 0.24841 | 0.10128 | 0.43000 | 0.99695 |
| 2.6 | 0.82055 | 0.27941 | 0.094348 | 0.46000 | 0.99656 |
| 2.8 | 0.80439 | 0.29562 | 0.083767 | 0.45000 | 0.99714 |
| 3.0 | 0.78652 | 0.31348 | 0.074624 | 0.46000 | 0.99738 |
| 3.2 | 0.76984 | 0.33011 | 0.073808 | 0.49 | 0.99869 |
| 3.4 | 0.75452 | 0.34548 | 0.066045 | 0.50000 | 0.99812 |
| 3.6 | 0.74414 | 0.35586 | 0.068060 | 0.52000 | 0.99751 |
| 3.8 | 0.78377 | 0.41623 | 0.061514 | 0.52000 | 0.99713 |
| 4.0 | 0.54936 | 0.20064 | 0.053413 | 0.52000 | 0.99847 |
| 4.2 | 0.61743 | 0.28256 | 0.048133 | 0.54000 | 0.99843 |
| 4.4 | 0.53755 | 0.21245 | 0.037174 | 0.51000 | 0.99857 |
| 4.6 | 0.53388 | 0.21612 | 0.028233 | 0.50000 | 0.99580 |
| 4.8 | 0.56107 | 0.23893 | 0.016400 | 0.39000 | 0.98326 |
| 5.0 | 0.5617 | 0.2383 | 0.0098590 | 0.34000 | 0.98592 |
| 5.2 | 0.53761 | 0.21239 | 0.0054973 | 0.31000 | 0.98575 |
| 5.4 | 0.53451 | 0.21549 | 0.0031805 | 0.31000 | 0.98704 |
| 5.6 | 0.53571 | 0.21429 | 0.0018401 | 0.24000 | 0.99646 |
| 5.8 | 0.53426 | 0.21574 | 0.0010780 | 0.22000 | 0.99810 |
| 6.0 | 0.53404 | 0.21596 | 0.00061507 | 0.21000 | 0.99832 |
| 6.2 | 0.48428 | 0.16586 | 0.00038624 | 0.20000 | 0.99838 |
| 6.4 | 0.5323 | 0.2177 | 0.00024245 | 0.17000 | 0.99937 |
| 6.6 | 0.52966 | 0.22034 | 0.00016413 | 0.16000 | 0.99917 |
| 6.8 | 0.53041 | 0.21959 | 0.00011605 | 0.11000 | 0.99923 |

Theoretical calculations

Table S6. Matrix representative of the spin-orbit Hamiltonian of equation 2.

$$(\hat{H}_{SOC}) = \begin{matrix} & \begin{matrix} |xz, -2\rangle & |xz, -1\rangle & |xz, 0\rangle & |xz, 1\rangle & |xz, 2\rangle & |yz, -2\rangle & |yz, -1\rangle & |yz, 0\rangle & |yz, 1\rangle & |yz, 2\rangle \end{matrix} \\ \begin{pmatrix} -\delta_1 & 0 & 0 & 0 & 0 & i(\zeta/2)+\delta_2 & 0 & 0 & 0 & 0 \\ 0 & -\delta_1 & 0 & 0 & 0 & 0 & -i\zeta/4+\delta_2 & 0 & 0 & 0 \\ 0 & 0 & -\delta_1 & 0 & 0 & 0 & 0 & \delta_2 & 0 & 0 \\ 0 & 0 & 0 & -\delta_1 & 0 & 0 & 0 & 0 & i\zeta/4+\delta_2 & 0 \\ 0 & 0 & 0 & 0 & -\delta_1 & 0 & 0 & 0 & 0 & -i\zeta/2+\delta_2 \\ -i\zeta/2+\delta_2 & 0 & 0 & 0 & 0 & \delta_1 & 0 & 0 & 0 & 0 \\ 0 & i\zeta/4+\delta_2 & 0 & 0 & 0 & 0 & \delta_1 & 0 & 0 & 0 \\ 0 & 0 & \delta_2 & 0 & 0 & 0 & 0 & \delta_1 & 0 & 0 \\ 0 & 0 & 0 & -i\zeta/4+\delta_2 & 0 & 0 & 0 & 0 & \delta_1 & 0 \\ 0 & 0 & 0 & 0 & i\zeta/2+\delta_2 & 0 & 0 & 0 & 0 & \delta_1 \end{pmatrix} \end{matrix}$$

Table S7. Matrix representative of the ZFS Hamiltonian given in equation 4 in the basis of the Ms components of the spin S = 2.

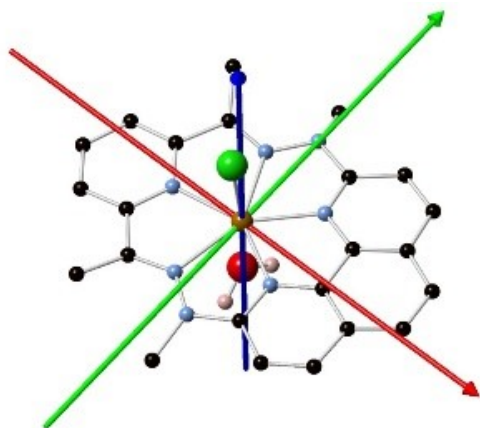
$$(\hat{H}_{ZFS}) = \begin{matrix} & \begin{matrix} |-2\rangle & |-1\rangle & |0\rangle & |1\rangle & |2\rangle \end{matrix} \\ \begin{pmatrix} 2D + 12B_{40} & 0 & \sqrt{6}E & 0 & 0 \\ 0 & -D - 48B_{40} & 0 & 3E & 0 \\ \sqrt{6}E & 0 & -2D + 72B_{40} & 0 & \sqrt{6}E \\ 0 & 3E & 0 & -D - 48B_{40} & 0 \\ 0 & 0 & \sqrt{6}E & 0 & 2D + 12B_{40} \end{pmatrix} \end{matrix}$$

Table S8. Values for g_x , g_y , and g_z of complexes **1-4**.

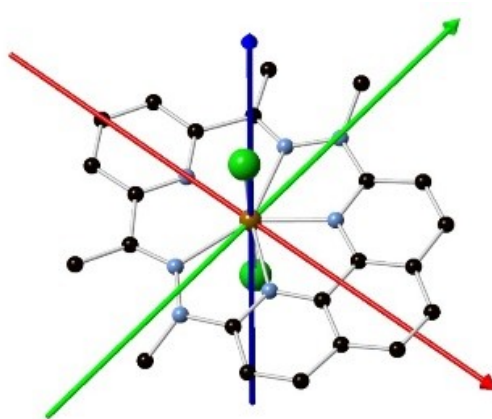
| Complex | g_x | g_y | g_z |
|--------------------------------|-------|-------|-------|
| 1 (Cl H ₂ O) | 1.99 | 2.07 | 2.34 |
| 2 (Cl ₂) | 1.84 | 1.87 | 2.57 |
| 3 (Br ₂) | 1.77 | 1.83 | 2.59 |
| 4 (I ₂) | 1.76 | 1.80 | 2.59 |

Figure S15. View of the **D** tensor proper axes for **1**, and of the **g** tensor in the other complexes; x in red, y in green, and z in blue of complexes 1-4.

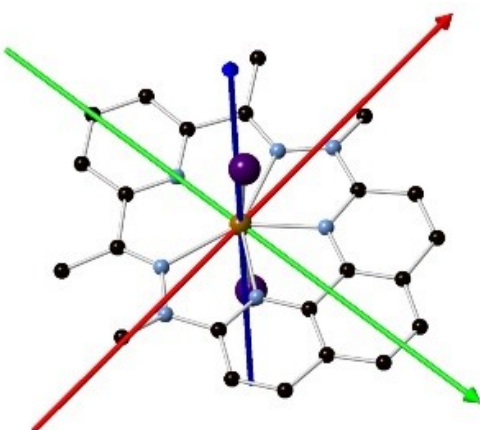
1



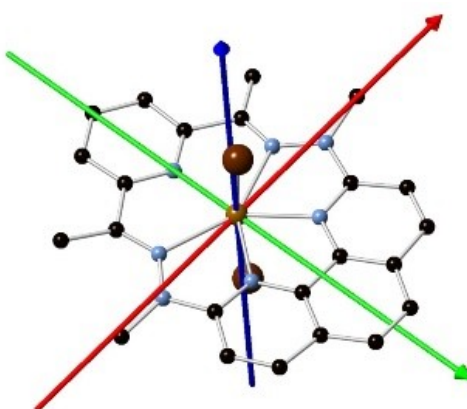
2



3



4



REFERENCES

1. O. Kahn, *Molecular Magnetism*, VCH, Weinheim, 1993.
2. N. F. Chilton, R. P. Anderson, L. D. Turner, A. Soncini and K. S. Murray, PHI: A powerful new program for the analysis of anisotropic monomeric and exchange-coupled polynuclear d- and f-block complexes, *J. Comput. Chem.*, 2013, **34**, 1164-1175.
3. N. F. Chilton, R. P. Anderson, L. D. Turner, A. Soncini and K. S. Murray, PHI, *J. Comput. Chem.*, 2013, **34**, 1164 – 1175.
4. Agilent, *CrysAlis PRO*, Agilent Technologies Ltd, Yarnton, Oxfordshire, England, 2014
5. V. Petříček, M. Dušek and L. Palatinus, Crystallographic Computing System JANA2006: General features, *Z. Krist.*, 2014, **229**, 345-352.
6. L. Palatinus and G. Chapuis, Superflip, *J. Appl. Cryst.*, 2007, **40**, 786-790.
7. V. Petříček, L. Palatinus, J. Plášil and M. Dušek, Jana2020 – a new version of the crystallographic computing system Jana, *Z. Krist.*, 2023, **238**, 271-282.
8. M. Llunell, D. Casanova, J. Cirera, P. Alemany and S. Alvarez, *SHAPE: Program for the stereochemical analysis of molecular fragments by means of continuous shape measures and associated tools*, University of Barcelona, Barcelona, 2013
9. D. Casanova, P. Alemany, J. M. Bofill and S. Alvarez, Shape and symmetry of heptacoordinated transition-metal complexes: structural trends, *Chem. Eur. J.*, 2003, **9**, 1281-1295.
10. C. Dekker, A. F. M. Arts, H. W. de Wijn, A. J. van Duynveldt and J. A. Mydosh, Activated dynamics in a two-dimensional Ising spin glass: $\text{Rb}_2\text{Cu}_{1-x}\text{Co}_x\text{F}_4$, *Phys. Rev. B*, 1989, **40**, 11243.